

Images of shadow and thin accretion disk around Bardeen black hole surrounded by perfect fluid dark matter

Haiyuan Feng ^{a,1,†} Ziqiang Cai,^{2,‡} Hao-Peng
Yan,^{3,§} Rong-Jia Yang,^{4,¶} and Jinjun Zhang ^{f1,††}

¹School of Physics and Electronic Engineering,
Shanxi Normal University, Taiyuan 030031, China

²School of Physics, Guizhou University, Guiyang 550025, China

³College of Physics, Taiyuan University of Technology, Taiyuan 030024, China

⁴College of Physical Science and Technology,
Hebei University, Baoding 071002, China

Abstract

We investigated the shadow and optical appearance of Bardeen black hole (BH) immersed in perfect-fluid dark matter (PFDM). Using the EHT data, we find that the DM parameter is restricted to a narrow allowed range, confined to values of $\mathcal{O}(10^{-1} - 10^{-2})$. Additionally, we observed that increasing the DM parameter substantially enlarges the photon sphere, the critical impact parameter, and thus the shadow radius, whereas the magnetic charge g produces only negligible corrections. The DM component also modifies the optical appearance of the accretion disk: higher b systematically suppresses the observed radiation intensity and reduces image brightness, while changes in g yield only marginal effects. Subsequently, using the Novikov–Thorne thin disk model, we analyze primary and secondary images, observed flux, and redshift patterns, showing that PFDM noticeably alters image size and brightness whereas magnetic charge has a negligible influence. No blueshifted regions appear in any configuration. These results highlight several promising observational signatures for testing DM environments and nonlinear electrodynamic effects around BHs.

^a Corresponding author

^f Corresponding author

[†] Email address: fenghaiyuan@sxnu.edu.cn

[‡] Email address: gs.zqcai24@gzu.edu.cn

[§] Email address: yanhaopeng@tyut.edu.cn

[¶] Email address: yangrongjia@tsinghua.org.cn^f

^{††} Email address: zhangjinjun@sxnu.edu.cn

I. INTRODUCTION

The pioneering observations by the Event Horizon Telescope (EHT) collaboration have ushered in a new era of black hole (BH) imaging and strong-field gravity studies. The release of the first image of the supermassive BH M87* in 2019 [1–6] marked a major milestone, sparking extensive investigations into BH shadows as powerful probes for testing gravitational theories and exploring the electromagnetic characteristics of compact objects [7–20]. More recently, in May 2022, the EHT collaboration presented the image of Sgr A*, the supermassive BH at the center of the Milky Way, revealing an asymmetric emission ring [21–26]. These successive advancements have greatly enhanced the statistical robustness of BH shadow observations, offering a promising avenue to place stringent constraints on alternative BHs that deviate from the standard Kerr paradigm [27]. Motivated by these observational breakthroughs, it has become essential to understand how the intrinsic properties of BHs and their surrounding environments influence the formation and morphology of the observed shadow.

The BH shadows represent one of the most striking observational signatures of strong gravitational fields. It appears as a dark region surrounded by a bright emission ring, formed by the gravitational lensing and photon capture effects near the event horizon. For a non-rotating BH, such as the Schwarzschild BH (Sch BH), the shadow exhibits a perfectly circular boundary. This property was originally analyzed by Synge and later extended by Luminet, who explored how the presence of thin accretion disk modifies the observed shadow [28, 29]. In contrast, the shadow produced by a rotating BH, such as the Kerr BH, becomes asymmetric and deformed as a result of spin-induced frame-dragging effects [30, 31]. The morphology of the shadow is determined by the specific spacetime geometry surrounding BH. In recent decades, a substantial body of research has focused on analyzing shadow characteristics across diverse BHs, both within the framework of GR and in various modified gravity theories [18, 32–52]. These studies highlight that the remarkable success of the EHT in imaging BH shadows has inaugurated a new frontier in observational relativity.

Moreover, imaging techniques for thin accretion disks—ranging from semi-analytic approaches to advanced ray-tracing methods coupled with radiative transfer—serve as a powerful tool for testing gravity in the strong-field regime. Building upon the classical Shakura–Sunyaev model for geometrically thin and optically thick disks and its relativistic gener-

alization by Novikov and Thorne [53, 54], semi-analytic analyses such as that of Lunin et al. have provided direct and secondary disk images along with analytical predictions for radiation flux, while modern numerical ray-tracing simulations have enabled realistic modeling of accretion-disk images in a variety of BHs [15, 55–68]. Although the geometric outline of the shadow is primarily determined by the spacetime structure rather than the detailed accretion dynamics, the observed luminosity distribution, ring morphology, and photon ring substructures are highly sensitive to the emission of thin accretion disks and radiative processes [69–76]. Therefore, by combining physically consistent disk models with realistic radiative transfer and high-precision ray-tracing techniques, accretion-disk imaging also provides a robust observational framework to probe strong-field gravity and to discriminate between GR and its possible modifications.

Recent observations have yet to definitively exclude deviations from GR, leaving open the possibility of testing alternative theories of gravity. The existence of spacetime singularities, signaling the breakdown of GR, has prompted extensive efforts to formulate regular model through quantum corrections and gravitational modifications [77–83]. In this context, Bardeen proposed the non-singular BH solution, later understood as arising from the gravitational collapse of magnetic monopoles within a nonlinear electrodynamics framework [84, 85]. This pioneering work stimulated the development of other regular BH models, including those of Hayward and Ayón-Beato–García, which successfully remove curvature singularities while maintaining physical consistency [86–88]. The dynamical behavior, quasinormal spectra, lensing signatures, and particle trajectories associated with such regular geometries have been comprehensively analyzed in recent years, offering insights into strong-field gravitational phenomena [89–93].

In another context, observations of galaxy cluster dynamics have long pointed to the existence of an unseen mass component in the universe. Zwicky’s pioneering analysis of Cluster first uncovered a significant mismatch between the luminous and gravitational mass, giving rise to the dark matter (DM) hypothesis—later substantiated by studies of galactic systems and other clusters [94–97]. Although DM eludes direct electromagnetic detection, strong indirect evidence from flat galactic rotation curves, cluster dynamics, and cosmic microwave background anisotropies firmly supports its presence [95, 98]. Beyond its cosmological significance, DM can influence the spacetime geometry and accretion dynamics around compact objects, with recent studies suggesting that superradiant instabilities and axion-like DM ac-

cretion near BHs may yield detectable gravitational wave signatures [99–101]. Consequently, the impact of DM is non-negligible. In this study, we examine the shadow and observable intensity of Bardeen BH immersed in perfect fluid dark matter (PFDM-Bardeen BH), with an optically thin disk accretion serving as the background light source. We will explore how the magnetic monopole charge and DM parameter influence the shadow structure and emission properties. Such an analysis may provide a promising avenue to observationally distinguish PFDM-Bardeen geometry from Sch BH.

The structure of this paper is outlined as follows. Section 2 introduces the Bardeen BH surrounded by DM and discusses the theoretical constraints governing the existence of inner and outer horizons. Section 3 employs EHT observations to place bounds on the model parameters, with particular emphasis on the range and magnitude of the DM parameter. In Section 4, we classify photon trajectories into direct emission, lensing rings, and photon rings, and examine how the model parameters influence various associated physical quantities, including the transfer function and intensity distribution. Section 5 investigates the primary and secondary images of the accretion disk, focusing on the behavior of the observed radiation flux and redshift, and analyzes how the parameters shape the optical appearance of the disk. The final section provides a summary of our main conclusion.

II. BARDEEN BLACK HOLE SURROUNDED BY PERFECT FLUID DARK MATTER

The Bardeen BH stands as a representative example of a regular, singularity-free solution. First proposed by Bardeen in 1968 as a theoretical counterexample to the notion that gravitational collapse inevitably leads to a singularity concealed by an event horizon [84, 102], it challenged the classical understanding of BH interiors. Decades later, Ayón-Beato and García provided a physical foundation for this model by demonstrating that it arises as an exact solution to Einstein’s equations coupled with nonlinear electrodynamics (NLED), corresponding to the gravitational field generated by a magnetic monopole [85]. This reinterpretation transformed the Bardeen metric from a purely phenomenological construct into a physically consistent spacetime endowed with well defined matter source.

The geometry of Bardeen BH is characterized by the following metric

$$ds^2 = -\left(1 - \frac{2Mr^2}{(r^2 + g^2)^{3/2}}\right)dt^2 + \left(1 - \frac{2Mr^2}{(r^2 + g^2)^{3/2}}\right)^{-1}dr^2 + r^2d\Omega^2, \quad (1)$$

here the parameters M and g correspond to the ADM mass and the magnetic monopole charge, respectively. The angular part of the metric, $d\Omega^2 = d\theta^2 + \sin^2\theta d\phi^2$, represents the standard line element on a unit two-sphere. Unlike the Reissner–Nordström case, where the charge contribution falls off as $1/r^2$, the Bardeen modification introduces $1/r^3$ dependence. This higher-order decay ensures that all curvature invariants—including R , $R_{\mu\nu}R^{\mu\nu}$, and $R_{\mu\nu\alpha\beta}R^{\mu\nu\alpha\beta}$ —remain finite even at the origin $r = 0$. As a result, the Bardeen metric successfully eliminates the curvature singularity while still admitting the presence of event horizons. Solving the equation governing the existence of inner and outer horizons yields a critical magnetic charge of $g/M = 0.7698$, at which the two horizons merge at $r_+/M = r_-/M = r_*/M = 1.08866$. Consequently, the spacetime admits two distinct horizons when $g/M \in (0, 0.7698)$, whereas for values of g/M exceeding this limit, no horizon is present.

From physical perspective, the regular nature of Bardeen BH arises from the interaction between gravity and a nonlinear electromagnetic field, which is described by the Lagrangian $\mathcal{L}(F)$

$$\mathcal{L}(F) = \frac{3M}{|g|^3} \left(\frac{\sqrt{2g^2 F}}{1 + \sqrt{2g^2 F}} \right)^{\frac{5}{2}}, \quad (2)$$

which satisfies $F_{\mu\nu} = \nabla_\mu A_\nu - \nabla_\nu A_\mu$, with $\mathcal{L}(F)$ being a function of the electromagnetic invariant $\frac{1}{4}F_{\mu\nu}F^{\mu\nu}$. Incorporating PFDM into the Bardeen BH provides a natural framework to examine the interplay between DM and regular BHs. As PFDM captures the large scale DM distribution influencing galactic and BH environments, its inclusion enables an assessment of how DM modifies the horizon structure and thermodynamic properties of the Bardeen BH. Assuming the BH is embedded in PFDM background, Zhang et al. [103] derived the corresponding PFDM-Bardeen BH by coupling gravity with nonlinear electromagnetic field, for which the energy momentum tensor is given by

$$T^\mu_\nu = \text{diag}(-\rho, p_r, p_\theta, p_\phi), \quad (3)$$

with

$$\rho = -p_r = \frac{b}{r^3}, \quad p_\theta = p_\phi = \frac{b}{2r^3}, \quad (4)$$

where ρ , p_r , and $p_\theta = p_\phi$ denote the energy density, radial pressure, and tangential pressures of DM, respectively [104, 105]. The weak energy condition $T_{tt} \geq 0$ requires $b \geq 0$ [103]. The DM parameter b characterizes the local DM density and its dynamical effect on the spacetime geometry near BH, rather than the global cosmological DM content. Observationally, b

can be constrained by comparing theoretical predictions—such as galaxy rotation curves or BH shadow sizes—with astrophysical data. In the following section, we constrain these parameters using the observational data from EHT.

Moreover, since the BH under consideration is static and spherically symmetric, the corresponding metric can be represented as

$$ds^2 = -f(r)dt^2 + f(r)^{-1}dr^2 + r^2d\Omega^2, \quad (5)$$

and

$$f(r) = 1 - \frac{2Mr^2}{(r^2 + g^2)^{\frac{3}{2}}} - \frac{b}{r} \ln \frac{r}{|b|}. \quad (6)$$

It is clear from the above expression that setting both the DM parameter $b = 0$ and the magnetic charge $g = 0$ recovers the Sch BH. When DM is absent ($b = 0$), the metric reduces to the standard Bardeen BH, whereas vanishing magnetic charge ($g = 0$) corresponds to the Sch BH immersed PFDM (PFDM-Sch BH).

Figure 1 illustrates the regions where the inner and outer horizons of the PFDM-Bardeen BH exist. The red area denotes the presence of both horizons, the white area corresponds to naked singularity, and the blue boundary represents the extremal BH. In this context, the extremal condition is governed by the equations $f(r_*, g, b) = 0$ and $f'(r_*, g, b) = 0$ ($r_* = r_+ = r_-$), which together define a boundary curve in the (b, g) parameter plane that separates the BH domain from the naked singularity region.

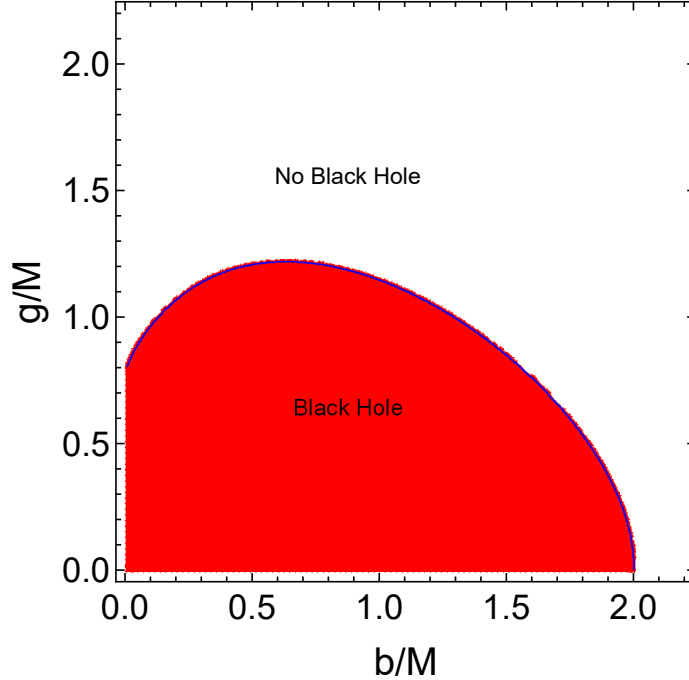


FIG. 1: On the horizontal axis, we have dimensionless DM parameter b/M , while the vertical axis represents the dimensionless magnetic charge g/M . The red area corresponds to the BH region, whereas the white area denotes the naked singularity.

III. CONSTRAINING MODEL PARAMETERS USING EHT OBSERVATIONS OF M87* AND SGR A*

Following the EHT observations of supermassive BH M87* and Sgr A* [1, 21], the apparent diameter of BH shadow provides a powerful probe to constrain model parameters in various modified gravity. Furthermore, we employ the measured shadow diameters of M87* and Sgr A* to place constraints on the DM parameter b . By comparing the theoretical prediction of the shadow diameter d_{sh} with the EHT observational ranges, we will determine the allowed parameter region consistent with observational uncertainties.

A. Null geodesic equation for Bardeen BH surrounded by PFDM

The photon sphere, defined as the unstable circular orbit of photons, delineates the boundary between light rays escaping to infinity and those captured by BH. Consequently, the apparent shadow observed by a distant observer is governed by the geometry of these null

trajectories. In the context of the PFDM-Bardeen BH, the interplay between the magnetic charge and the DM parameter significantly influences the radius of the photon sphere and the corresponding shadow size. To explore these effects, we derive the null geodesic equation in this BH and analyze the resulting photon dynamics.

The Lagrangian \mathcal{L} for a point particle in the spacetime (5) is given by

$$\mathcal{L} = \frac{1}{2} g_{\mu\nu} \frac{dx^\mu}{d\lambda} \frac{dx^\nu}{d\lambda}, \quad (7)$$

where λ represents the affine parameter. Owing to the spacetime's spherical symmetry, the motion of the particle can, without loss of generality, be restricted to the equatorial plane ($\theta = \pi/2$). Under this condition, two conserved quantities naturally emerge

$$\begin{cases} E = -g_{tt} \frac{dt}{d\lambda} = f(r) \frac{dt}{d\lambda}, \\ L = g_{\phi\phi} \frac{d\phi}{d\lambda} = r^2 \frac{d\phi}{d\lambda}. \end{cases} \quad (8)$$

For $\mathcal{L} = 0$, by combining Eqs. (7) and (8), one obtains the governing equations that describe the propagation of light in this BH

$$\begin{cases} \frac{dt}{d\lambda'} = \frac{1}{\bar{b}f(r)}, \\ \frac{d\phi}{d\lambda'} = \frac{1}{r^2}, \\ \left(\frac{dr}{d\lambda'} \right)^2 = \frac{1}{\bar{b}^2} - \frac{f(r)}{r^2}, \end{cases} \quad (9)$$

here, we redefine the affine parameter as $\lambda' = L\lambda$, while $\bar{b} = L/E$ represents the impact parameter associated with the photon trajectory. This parameter holds fundamental importance, as it directly determines the photon's trajectory and, consequently, the shape and size of BH shadow. Physically, the impact parameter characterizes the perpendicular distance between the photon's initial direction and the BH's center, thus governing whether the photon will escape to infinity, orbit in the photon sphere, or be captured by the event horizon.

By manipulating the light propagation equation, the radial coordinate r can be expressed as an ordinary differential equation with respect to the azimuthal angle ϕ within the orbital plane

$$\left(\frac{dr}{d\phi} \right)^2 = r^4 \left(\frac{1}{\bar{b}^2} - \frac{f(r)}{r^2} \right) \equiv V_{\text{eff}}, \quad (10)$$

where V_{eff} represents the effective potential governing photon motion, and the left-hand side corresponds to the kinetic energy term in Newtonian dynamics. To facilitate the analysis of photon trajectories, we define a new variable $u = 1/r$, which allows the photon's equation of motion to be recast in the following form

$$\left(\frac{du}{d\phi}\right)^2 = \frac{1}{\bar{b}^2} - u^2 f\left(\frac{1}{u}\right) \equiv G(u). \quad (11)$$

Figure 2 depicts the dependence of $G(u)$ on u for magnetic charge $g/M = 0.5$ and DM parameter $b/M = 1$. The plot clearly reveals the existence of a critical impact parameter \bar{b}_c that distinguishes different photon trajectories. For $\bar{b} > \bar{b}_c$, photons arriving from spatial infinity are gravitationally deflected, reaching a minimum radial distance r_{min} before escaping back to infinity (where r_{min} denotes the closest radial distance of the photon from the BH during its motion). When $\bar{b} < \bar{b}_c$, photons are inevitably captured by PFDM-Bardeen BH, defining the photon capture cross-section. At the threshold $\bar{b} = \bar{b}_c$, photons follow unstable circular orbits around PFDM-Bardeen BH, with the corresponding orbital radius identified as the photon sphere radius.

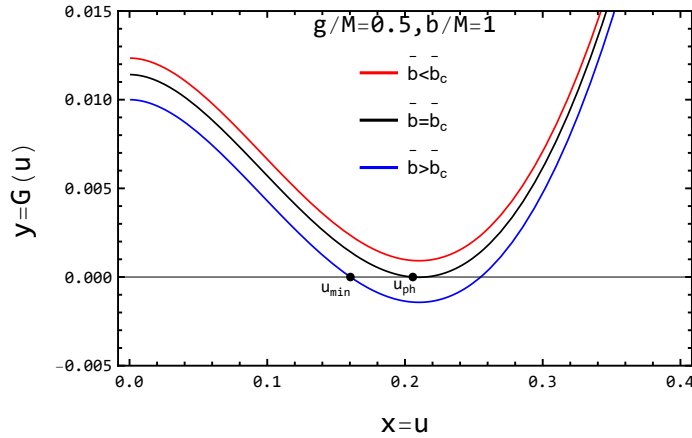


FIG. 2: The functions $G(u)$ for different values of \bar{b} , as a function of u .

Figure 3 illustrates the dependence of the photon sphere radius r_{ph} on the magnetic charge g and the DM parameter b . As shown in the left panel, for a fixed magnetic charge g , increasing b causes r_{ph} to increase initially, reach a peak, and then decrease, indicating a non-monotonic relationship. In contrast, for a fixed b , the variation with respect to g is relatively weak. A more detailed inspection reveals that a larger magnetic charge slightly decreases r_{ph} , and the r_{ph} of the PFDM-Sch BH remains consistently larger than that of the

PFDM–Bardeen BH. The right panel further demonstrates that the influence of g remains modest: within a certain range, an increase in b at constant g enlarges r_{ph} , while the Bardeen BH consistently exhibits a smaller r_{ph} than its PFDM–Bardeen counterpart.

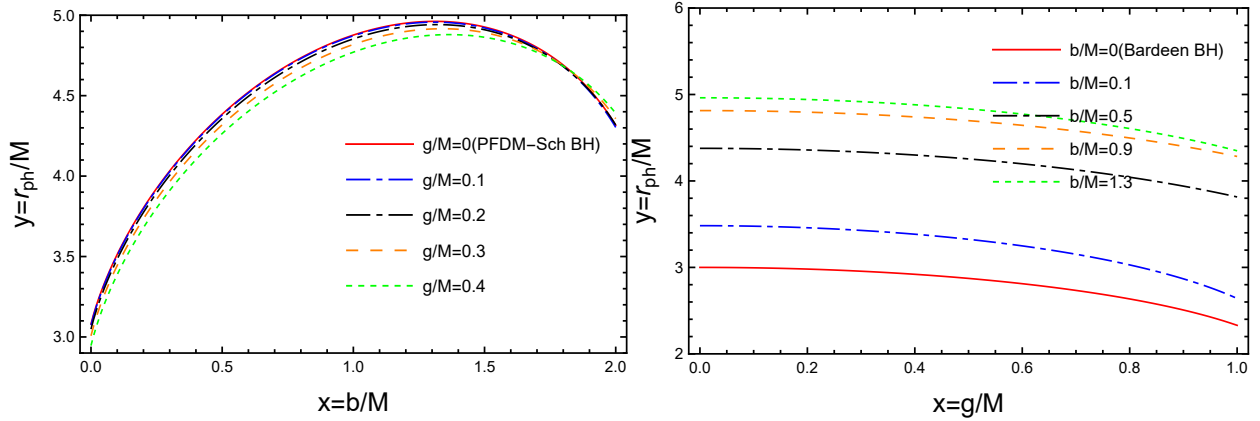


FIG. 3: The two pictures illustrate the dependence of photon sphere radius on the magnetic charge g and DM parameter b .

To determine the critical impact parameter \bar{b}_c , we first consider the case $\bar{b} > \bar{b}_c$. In this scenario, when the photon reaches its point of closest approach to the BH ($r = r_{\text{min}}$), the relation $\bar{b} = \frac{r_{\text{min}}}{\sqrt{f(r_{\text{min}})}}$ holds. As $r \rightarrow r_{\text{ph}}$, the impact parameter approaches its critical value \bar{b}_c . To identify the radius of the photon sphere, we note that for circular photon orbits the conditions $\dot{r} = 0$ (zero radial velocity) and $\ddot{r} = 0$ (zero radial acceleration) must be satisfied, which are equivalent to $V_{\text{eff}}|_{r=r_{\text{ph}}} = 0$ and $dV_{\text{eff}}/dr|_{r=r_{\text{ph}}} = 0$, respectively. At this stage, the critical impact parameter \bar{b}_c , corresponding to the photon sphere, can be determined by

$$\bar{b}_c = \frac{r_{\text{ph}}}{\sqrt{f(r_{\text{ph}})}}. \quad (12)$$

It should be emphasized that the critical impact parameter is fundamentally linked to the radius of BH shadow. The shadow structure can be examined by tracing light rays backward in time from a static observer located at radial coordinate r_o . The shadow boundary is defined by those light rays that asymptotically approach the unstable circular photon orbits at r_{ph} . For a general static, spherically symmetric, and asymptotically flat spacetime, Ref. [106, 107] demonstrated that when the observer is sufficiently distant from BH ($r_o \rightarrow \infty$), the apparent shadow radius tends to the critical impact parameter \bar{b}_c . Consequently, this radius is governed by the position of the photon sphere and the form of the metric function $f(r)$.

B. Constraining DM parameter via shadow diameter

Based on the physical implications of Eq. (12), this subsection provides stringent constraints on the DM parameter using the EHT observations of supermassive BHs M87* and Sgr A*. For M87*, general-relativistic magnetohydrodynamic (GRMHD) simulations indicate that current EHT data cannot effectively distinguish whether the BH is rotating or spherically symmetric based solely on shadow morphology [108]. The measured shadow size remains consistent with $3\sqrt{3}(1 \pm 0.17)M$, independent of whether the model assumes spherical or axisymmetric symmetry [109]. Additionally, for Sgr A*, the spin parameter is sufficiently small such that its influence on the shadow radius can be safely neglected [110]. Accordingly, constraints on the PFDM–Bardeen BH can be established using current EHT observations.

For M87*, the observed shadow exhibits an angular diameter of $42 \pm 3 \mu\text{as}$, corresponding to a source located approximately 16.8 Mpc away, with a central BH mass estimated at $(6.5 \pm 0.9) \times 10^9 M_\odot$ [1]. Meanwhile, for Sgr A*, the EHT collaboration reported angular diameter $48.7 \pm 7 \mu\text{as}$, with the Galactic Center situated at a distance of $8277 \pm 33 \text{ pc}$ and harboring a supermassive BH of mass $(4.3 \pm 0.013) \times 10^6 M_\odot$ [21].

The shadow diameter, expressed in units of mass, can be evaluated from the BH parameters through relation

$$d_{\text{sh}} = \frac{D\theta}{M}, \quad (13)$$

where D represents the distance from the observer. Accordingly, the theoretical estimate of the radius of BH shadow is obtained using $d_{\text{sh}}^{\text{theo}} = 2R_{\text{sh}} = 2\bar{b}_c$. By applying this relation, we can determine the corresponding shadow diameters for M87* and Sgr A*, as presented by [65, 110]

$$\begin{cases} d_{\text{sh}}^{\text{M87*}} = (11 \pm 1.5)M, \\ d_{\text{sh}}^{\text{Sgr.A*}} = (9.77 \pm 0.67)M. \end{cases} \quad (14)$$

In Fig. 4, stringent constraints on the parameter b are derived under the condition that both the inner and outer horizons exist. The left panel illustrates the parameter constraints inferred from the shadow diameter of M87* within the 1σ and 2σ confidence intervals, where the red dashed curve corresponds to the 1σ range and the black dashed curve denotes the 2σ range. Likewise, the right panel presents the constraints obtained from the shadow diameter of Sgr A*. Furthermore, Table 1 summarizes the upper and lower bounds of parameter b

for both types of BHs at fixed magnetic charge g .

From the figure, it can be observed that the allowable range of g is primarily determined by its value at the outer horizon and the lower bound along the constraint curve, indicating that g possesses a definite lower limit. In contrast, the DM parameter b exhibits an upper bound, with its lower bound gradually emerging as g increases. As shown in Table 1, when $g = 0.7$ or 0.8 , both upper and lower limits of b appear within the 1σ confidence interval, while in other cases, only an upper limit is present. Based on these constraints, we infer that if PFDM–Bardeen BH truly exist, the surrounding DM parameter is likely constrained within the order of magnitude $O(10^{-1} - 10^{-2})$, as excessively large values are unlikely to be physically viable.

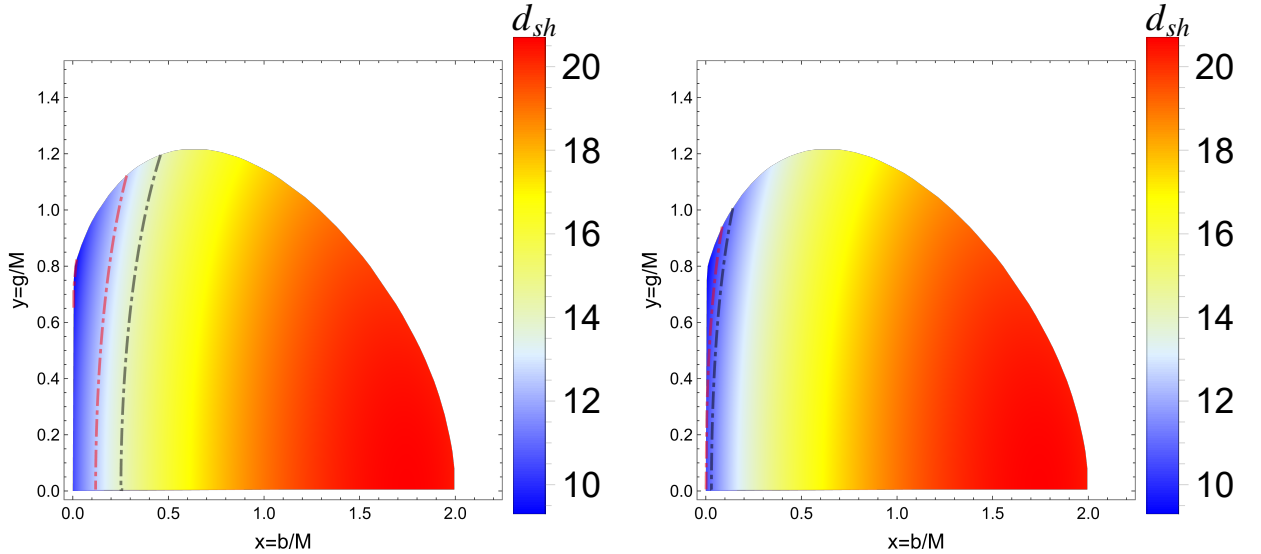


FIG. 4: The figure illustrates the contour plots of the shadow diameter within the theoretically allowed parameter space. (Left panel) The red dashed lines correspond to the M87* shadow diameter within the 1σ confidence interval, located at $d_{sh}/M = 9.5$ and $d_{sh}/M = 12.5$. The black dashed line represents the 2σ confidence interval at $d_{sh}/M = 14$. (Right panel) For Sgr A*, the red and black dashed lines similarly denote the 1σ and 2σ confidence regions, corresponding to shadow diameters $d_{sh}/M = 10.44$ and $d_{sh}/M = 11.11$, respectively.

TABLE I: The table presents the values of b/M at the 1σ and 2σ confidence levels for M87* and Sgr A*, with g held fixed.

M87*/b	1σ	1σ	2σ	2σ	Sgr A*/b	1σ	1σ	2σ	2σ
g	Upper	Lower	Upper	Lower	g	Upper	Lower	Upper	Lower
0.1M	0.12025	-	0.25262	-	0.1M	0.00151	-	0.03027	-
0.2M	0.12327	-	0.25602	-	0.2M	0.00324	-	0.03270	-
0.3M	0.12837	-	0.26176	-	0.3M	0.00630	-	0.03689	-
0.4M	0.13566	-	0.26992	-	0.4M	0.01105	-	0.04298	-
0.5M	0.14532	-	0.28066	-	0.5M	0.01788	-	0.05122	-
0.6M	0.15756	-	0.29419	-	0.6M	0.02720	-	0.06192	-
0.7M	0.17268	0.00322	0.31078	-	0.7M	0.03949	-	0.07547	-
0.8M	0.19109	0.01593	0.33082	-	0.8M	0.05537	-	0.09239	-

IV. OBSERVED APPEARANCE, SHADOW, AND PHOTON RINGS IN THIN DISK ACCRETION FLOW

In this section, we explore the optical appearance of the PFDM–Bardeen BH when it is illuminated by a geometrically thin, optically thick accretion disk [111–113]. The observer is assumed to be positioned along the polar axis, viewing the disk face-on in the equatorial plane. Photons emitted from various regions of the disk follow distinct trajectories, leading to different observable features in the BH image. To understand these effects, we first categorize the possible photon trajectories around PFDM–Bardeen BH before examining the corresponding image formation. Hence, within the parameter space constrained by current observational data, our analysis focuses on elucidating how the presence of the DM parameter and magnetic charge modifies photon propagation and the resulting image morphology.

A. Categories of photon trajectories: Direct emission, Lensing rings, and Photon rings

To establish the foundation for this investigation, we first analyze the trajectories of photons propagating in the vicinity of the BH. Equation (11) provides the general form of

the photon's trajectory. When the impact parameter satisfies $\bar{b} < \bar{b}_c$, the photon trajectory stays outside the event horizon. In this regime, the total variation of the azimuthal angle ϕ along the photon's path can be obtained by integrating the orbital equation

$$\phi = \int_0^{u_H} \frac{1}{\sqrt{G(u)}} du, \quad \bar{b} < \bar{b}_c, \quad (15)$$

the upper integration limit is $u_H = 1/r_H$, where r_H represents the radial position of the BH's outer event horizon. When $\bar{b} > \bar{b}_c$, the light ray experiences a turning point determined by the smallest positive real root of $G(u) = 0$ (This root is expressed as $u_{\min} = 1/r_{\min}$). Consequently, the total deflection angle of the photon, measured as the accumulated change in the azimuthal coordinate ϕ outside the event horizon, can be calculated through the integral form that depends on the specific value of the impact parameter \bar{b}

$$\phi = 2 \int_0^{u_{\min}} \frac{1}{\sqrt{G(u)}} du, \quad \bar{b} > \bar{b}_c. \quad (16)$$

To elucidate the origin of the radiation detected near BHs, photon trajectories are often divided into three distinct classes—direct emission, lensing ring, and photon ring—as initially proposed in Ref. [114]. Within this framework, one can characterize the orbital motion of photons by defining the turn number $n(\bar{b}) = \phi/2\pi$, which quantifies how many complete revolutions a photon performs around the BH prior to reaching the observer. The value of $n(\bar{b})$ depends sensitively on the impact parameter \bar{b} , and as demonstrated in Refs. [112, 113], it shows discrete transitions corresponding to different photon path families. The function $n(\bar{b})$ can be defined as

$$n(\bar{b}) = \frac{2m-1}{4}, \quad m \in \mathbb{Z}^+. \quad (17)$$

The boundaries separating the different photon trajectory families are determined by the critical impact parameters \bar{b}_m^\pm . Specifically, \bar{b}_m^- (with $\bar{b}_m^- < \bar{b}_c$) and \bar{b}_m^+ (with $\bar{b}_m^+ > \bar{b}_c$) represent, respectively, the smallest and largest allowed impact parameters associated with the m -th order photon orbits, where \bar{b}_c denotes the critical value. These parameters serve as thresholds that distinguish distinct classes of photon paths, which can be systematically categorized as

- direct emission: $\frac{1}{4} < n < \frac{3}{4} \Rightarrow \bar{b} \in (0, \bar{b}_2^-) \cup (\bar{b}_2^+, \infty)$;
- lensing ring: $\frac{3}{4} < n < \frac{5}{4} \Rightarrow \bar{b} \in (\bar{b}_2^-, \bar{b}_3^-) \cup (\bar{b}_3^+, \bar{b}_2^+)$;
- photon ring: $n > \frac{5}{4} \Rightarrow \bar{b} \in (\bar{b}_3^-, \bar{b}_3^+)$.

Direct emission corresponds to photons that travel from the accretion disk to the observer after a single intersection with the disk surface. In contrast, lensing rings arise from photons that undergo two disk crossings due to gravitational deflection before reaching the observer. Finally, photon rings are formed by photons that orbit the BH multiple times—intersecting the disk three or more times—before eventually escaping toward the observer, producing the innermost lensed features in observed image.

Figure 5 illustrates the photon trajectories for three BH spacetimes: the Bardeen BH ($g/M = 0.1$), the PFDM-Sch BH ($b/M = 0.1$), and the PFDM-Bardeen BH ($g/M = b/M = 0.1$). The first row shows how the orbital winding number around the thin accretion disk varies with the impact parameter \bar{b} , where red curves denote photon ring trajectories, yellow curves represent lensing ring trajectories, and black curves correspond to direct emission. The second row presents the associated photon paths, with direct emission shown in blue, lensing ring trajectories in green, and photon ring trajectories in red, thereby completing the classification of photon motion in these geometries. In addition, table II reveals clear quantitative distinctions among the Bardeen, PFDM-Sch, and PFDM-Bardeen BHs. The shadow radius \bar{b}_c shows clear and non-degenerate differences among the three BHs. As indicated in Table II, the Bardeen BH yields the smallest shadow scale, with $\bar{b}_c/M \approx 5.19$. When PFDM is introduced, the shadow becomes significantly larger: the PFDM-Bardeen and PFDM-Sch BHs give $\bar{b}_c/M \approx 6.11$ and 6.12 , respectively, representing an increase of about 17–18% relative to the Bardeen case. A similar hierarchy is observed for the other characteristic quantity: both r_H and r_{ph} consistently exceed the corresponding values of the Bardeen BH.

Table III shows how the DM parameter and the magnetic charge affect the horizon radius, photon sphere radius and the shadow scale. When the magnetic charge is fixed at $g/M = 0.1$, increasing the DM parameter b consistently enlarges the key geometrical scales of BH. The outer horizon shifts outward, the photon sphere radius increases, and the corresponding shadow radius becomes larger. This trend indicates that PFDM effectively deepens the gravitational potential at large radii, thereby expanding both the causal boundary and the region accessible to unstable photon orbits. In contrast, when the DM parameter is fixed at $b/M = 0.1$, variations in the magnetic charge exert only a modest influence. Increasing g slightly decreases the horizon radius, the photon sphere radius, and the shadow size, and these changes are significantly weaker than those driven by b . Overall, b serves as the primary

parameter governing the global BH scale and shadow diameter, while the magnetic charge introduces only a minor, secondary correction that mildly contracts these characteristic radii.

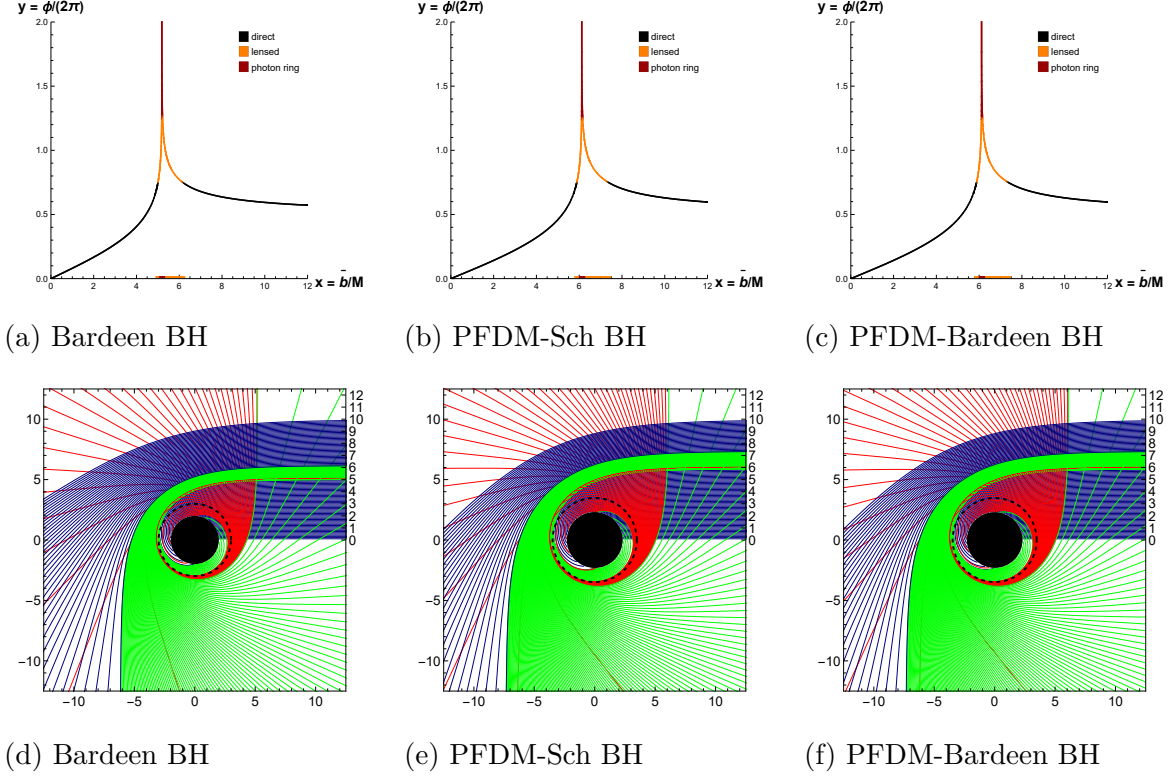


FIG. 5: The photon dynamics for the Bardeen, PFDM-Sch, and PFDM-Bardeen BHs are shown as functions of \bar{b} . The top panels display the winding number $n = \phi/2\pi$, used to classify trajectories: direct emission ($n < 3/4$, black), lensed ring ($3/4 < n < 5/4$, yellow), and photon ring ($n > 5/4$, red). The bottom panels illustrate representative paths in (r, ϕ) coordinates, with impact parameter $1/10$, $1/100$, and $1/1000$. The BH is shown as a filled disk, and the dashed circle marks the photon orbit. The three cases correspond to $g/M = 0.1$ (Bardeen BH), $b/M = 0.1$ (PFDM-Sch BH), and $b/M = 0.1, g/M = 0.1$ (PFDM-Bardeen BH).

B. Observed specific intensities inferred through transfer functions

To quantify the radiation received by a distant observer, we employ transfer functions, which encode the mapping between emission processes in the accretion flow and their corresponding appearance on the observer's screen. These functions incorporate the full general

TABLE II: Table summarizes the dimensionless physical quantities for the three BHs.

BHs	r_H/M	r_{ph}/M	\bar{b}_c/M	\bar{b}_1^-/M	\bar{b}_2^-/M	\bar{b}_2^+/M	\bar{b}_3^-/M	\bar{b}_3^+/M
Bardeen ($g/M = 0.1, b/M = 0.0$)	1.99247	2.99164	5.18747	2.83799	5.00485	6.16226	5.17897	5.21962
PFDM-Sch ($g/M = 0.0, b/M = 0.1$)	2.31416	3.48255	6.12047	3.30518	5.88831	7.36368	6.10897	6.16345
PFDM-Bardeen ($g/M = b/M = 0.1$)	2.30829	3.47608	6.11374	3.29758	5.88022	7.35976	6.10210	6.15704

TABLE III: Table examines how the model parameters affect various dimensionless physical quantities under two controlled scenarios: $g/M = 0.1$ or $b/M = 0.1$.

Magnetic charge $g/M=0.1$	r_H/M	r_{ph}/M	\bar{b}_c/M	\bar{b}_1^-/M	\bar{b}_2^-/M	\bar{b}_2^+/M	\bar{b}_3^-/M	\bar{b}_3^+/M
$b/M=0.00$ (Bardeen)	1.99247	2.99164	5.18747	2.83799	5.00485	6.16226	5.17897	5.21962
$b/M=0.04$	2.15297	3.23645	5.64572	3.07044	5.44002	6.74339	5.63586	5.68274
$b/M=0.08$	2.26149	3.40360	5.97039	3.22894	5.74579	7.16907	5.95933	6.01163
DM parameter $b/M=0.1$	r_H/M	r_{ph}/M	\bar{b}_c/M	\bar{b}_1^-/M	\bar{b}_2^-/M	\bar{b}_2^+/M	\bar{b}_3^-/M	\bar{b}_3^+/M
$g/M=0.00$ (PFDM-Sch)	2.31416	3.48255	6.12047	3.30518	5.88831	7.36368	6.10897	6.16345
$g/M=0.15$	2.30091	3.46794	6.10530	3.28803	5.87004	7.35485	6.09348	6.14901
$g/M=0.30$	2.26008	3.42313	6.05894	3.23515	5.81376	7.32820	6.04608	6.10501

relativistic effects experienced by photons—such as gravitational redshift, light bending, and multiple-orbit lensing—and therefore provide a direct bridge between the local emission of thin disk and observed specific intensity. By integrating the photon trajectories weighted by the appropriate transfer functions, one can systematically construct the observed brightness distribution, enabling a consistent comparison of BHs.

Following the setup of the previous subsection, we model the emission as originating from a geometrically thin, optically thin, and static accretion disk lying in the equatorial plane of PFDM-Bardeen BH, with isotropic local radiation. Photons are traced along null geodesics to a distant polar observer, who measures the radiation at frequency ν_o . The corresponding specific intensity is obtained through the relativistic transfer relation of Ref. [111–116], which follows

$$I_o(r, \nu_o) = f(r)^{\frac{3}{2}} I_e(r, \nu_e), \quad (18)$$

where $I_e(r, \nu_e)$ and ν_e denote the specific intensity and emission frequency at the disk surface, whereas $I_o(r, \nu_o)$ refers to the corresponding quantity measured by an observer at the north pole. The relation follows from Liouville's theorem, which guarantees that the quantity $I_e(r, \nu_e)/\nu_e^3$ remains conserved along photon geodesics. The total observed intensity $I_{\text{obs}}(r)$ at an image radius is subsequently obtained by integrating the observer frame specific intensity $I_o(r, \nu_o)$ over all frequencies.

$$I_{\text{obs}}(r) = \int I_o(r, \nu_o) d\nu_o = f(r)^2 I_{\text{em}}(r), \quad (19)$$

here the total emitted intensity defined as $I_{\text{em}}(r) = \int I_e(r, \nu_e) d\nu_e$, which represents the frequency integrated radiation output from each point on the disk. It should be stressed that the observed signal accounts only for radiation emitted by the disk, without including absorption, scattering, or reflection effects. Each time a photon trajectory intersects the equatorial plane, it acquires an additional contribution to the luminosity received by a distant observer. As outlined earlier, the degree of orbital winding determines the number of such intersections: weakly deflected rays cross the disk once, moderately wound trajectories intersect it twice after bending behind the BH, and highly wound paths encounter the disk three or more times as they loop around the compact object. The total observed intensity is therefore obtained by summing the emission gathered at each intersection along the photon path, yielding

$$I_{\text{obs}}(\bar{b}) = \sum_m f(r)^2 I_{\text{em}}(r) \Big|_{r=r_m(\bar{b})}, \quad (20)$$

where transfer function $r_m(\bar{b})$ provides a mapping between the photon impact parameter and the radial location at which the photon intersects the thin emitting disk. Its derivative $dr/d\bar{b}$, often referred to as the demagnification factor, quantifies how strongly the transfer function compresses or stretches this mapping. In essence, the slope characterizes the degree of demagnification encoded in the transfer function itself [114]. A steeper slope of the transfer function restricts the range of allowed impact parameters, thereby suppressing its contribution to the BH's total observed intensity. Although photons near the photon ring may, in principle, intersect the accretion disk multiple times, the extreme steepness of their transfer functions renders their intensity contribution effectively negligible. Consequently, our analysis focuses solely on the first three intersections ($m = 1, 2, 3$). The corresponding

transfer functions can be written as

$$\begin{cases} r_1(\bar{b}) = \frac{1}{u\left(\frac{\pi}{2}, \bar{b}\right)}, & \bar{b} \in (\bar{b}_1^-, +\infty), \\ r_2(\bar{b}) = \frac{1}{u\left(\frac{3\pi}{2}, \bar{b}\right)}, & \bar{b} \in (\bar{b}_2^-, \bar{b}_2^+), \\ r_3(\bar{b}) = \frac{1}{u\left(\frac{5\pi}{2}, \bar{b}\right)}, & \bar{b} \in (\bar{b}_3^-, \bar{b}_3^+). \end{cases} \quad (21)$$

Subsequently, we display these three classes of transfer functions in Fig. 6. The black curve denotes the first transfer function, whose nearly constant and relatively small slope produces the direct image of the emitting disk, reflecting the redshifted source profile. The Green curve corresponds to the second transfer function; its steep slope yields a strongly demagnified image originating from the far side of the disk, associated with the lensing ring. The red curve represents the third transfer function, characterized by an almost divergent slope, which generates an even more severely demagnified image from the front side of the disk, identified as the photon ring. Consequently, both the photon ring and lensing ring contributions are negligible in the total observed flux, with the direct emission overwhelmingly dominating the measured intensity.

In addition, we list the slopes $\tan \theta_b$, $\tan \theta_r$, and $\tan \theta_g$ corresponding to the black, red, and green curves in each panel. When focusing solely on the direct emission branch (black curve), the influence of the DM parameter b remains modest: Its increase produces only a slight reduction in the slope, which may in turn yield a modest enhancement in the observed brightness. In contrast, variations in the magnetic charge g generate changes that are even smaller—confined to the third decimal place and therefore negligible for practical purposes. Consequently, distinguishing the luminosity distributions of three BH configurations, as well as identifying how each parameter shapes the observed brightness, requires a more detailed analysis, which we carry out in the next subsection.

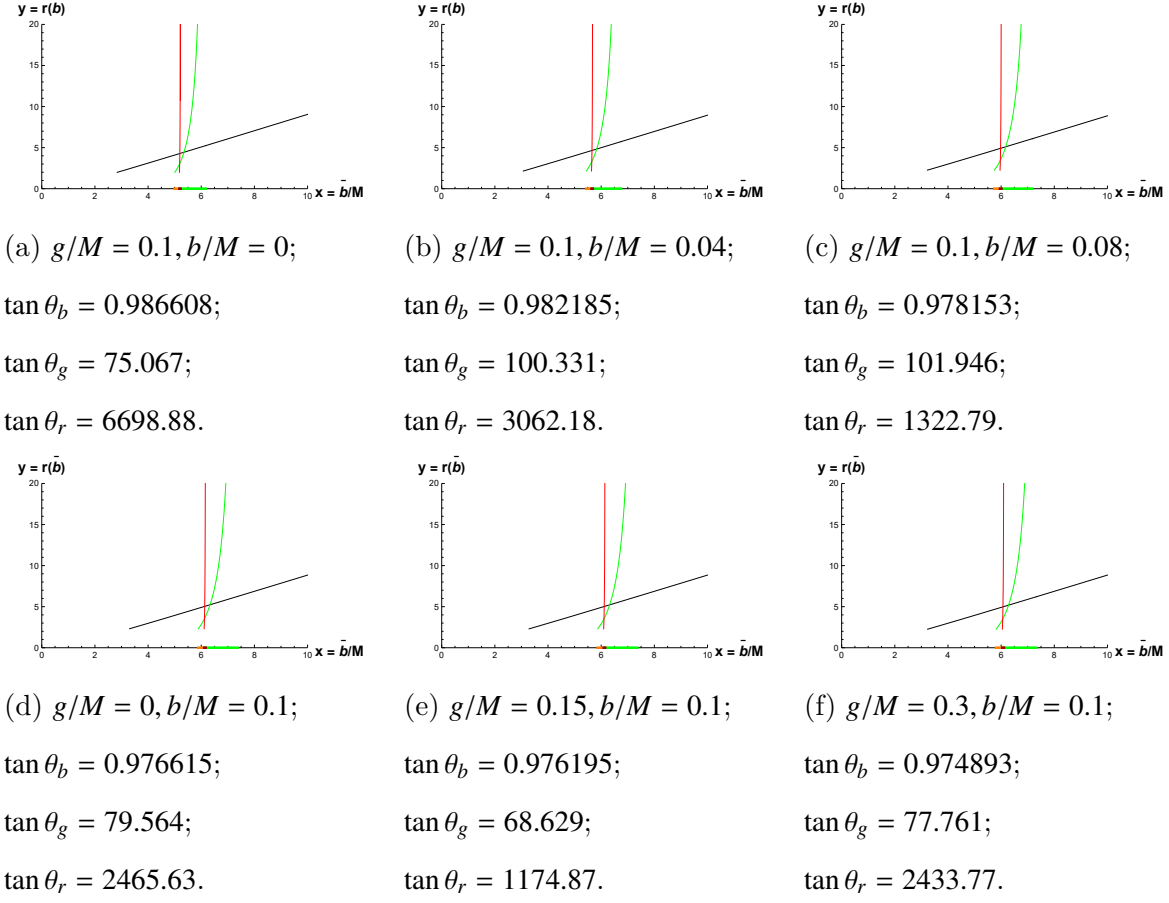


FIG. 6: The first three transfer functions for BHs with different parameter choices are displayed. The top row shows the cases $(g/M = 0.1, b/M = 0, 0.04, 0.08)$ from left to right, while the bottom row corresponds to $(g/M = 0, 0.15, 0.3, b/M = 0.1)$.

C. Optical appearance of PFDM-Bardeen BH with thin accretion disk

To investigate the optical appearance of the PFDM–Bardeen BH, we construct its observable image by projecting photon trajectories onto a two-dimensional screen placed at the observer’s location. Under various emission models, the visible structure of the spacetime is determined by how photons propagate in the strong-gravity region. In particular, the shadow boundary is defined by those rays that asymptotically spiral toward the unstable photon sphere. By tracing these critical geodesics from the vicinity of the BH and mapping them onto the observer’s image plane, we obtain the shadow silhouette expressed in the celestial coordinates. This procedure allows a direct visualization of how the PFDM param-

eter and magnetic charge modify both the shadow geometry and the surrounding brightness distribution.

Accordingly, once the emissivity profile of thin disk is specified, the received intensity can be evaluated through the transfer function formalism and then mapped onto the observer's image plane in celestial coordinates, yielding the full optical appearance of the BH. In our analysis, we explore three idealized, static emission models for the accretion disk. In the first emission model, the disk luminosity rises steeply from large radii and reaches the innermost stable circular orbit (r_{isco}), after which the profile transitions into a smooth quadratic falloff. In other words, the emission is sharply enhanced near the inner edge of the disk and then progressively diminishes as one moves outward.

$$I_{\text{em}}(r) = \begin{cases} I_0 \left(\frac{1}{r-(r_{\text{isco}}-1)} \right)^2, & r > r_{\text{isco}} \\ 0, & r < r_{\text{isco}} \end{cases} \quad (22)$$

where I_0 denotes the maximum value of the emitted intensity. In the second model, the emissivity is prescribed to peak precisely at the r_{ph} , after which it decreases following a cubic falloff. Thus, the brightest emission originates from the photon sphere region, with the intensity rapidly diminishing as the radius moves away from this location.

$$I_{\text{em}}(r) = \begin{cases} I_0 \left(\frac{1}{r-(r_{\text{ph}}-1)} \right)^3, & r > r_{\text{ph}} \\ 0, & r \leq r_{\text{ph}} \end{cases} \quad (23)$$

In the third model, the disk brightness decreases smoothly from the event horizon outward to the (r_{isco}). In this prescription, the emission gradually weakens across this radial range, producing a continuous, monotonic decline without a pronounced peak.

$$I_{\text{em}}(r) = \begin{cases} I_0 \frac{\frac{\pi}{2} - \arctan(r-(r_{\text{isco}}-1))}{\frac{\pi}{2} - \arctan(r_{\text{H}}-(r_{\text{isco}}-1))}, & r > r_{\text{H}} \\ 0. & r \leq r_{\text{H}} \end{cases} \quad (24)$$

Figures 7 and 8 display how the optical appearance of PFDM-Bardeen BH evolves as the DM parameter and magnetic charge. For each emission prescription, the first two columns illustrate the radial profiles of the intrinsic disk emissivity and the corresponding intensity measured by a distant observer. The final column translates these results into the observer's sky by mapping the radiation field onto the two-dimensional celestial coordinate plane, thereby showing the resulting images of the BH under each emission model. In Fig. 7, the

black curve represents the Bardeen BH, whereas the green, and red curves correspond to PFDM-Bardeen BH with $g/M = 0.1$ and DM parameter $b/M = 0.04$ and 0.08 , respectively. The key trends emerging from these comparisons are summarized below.

Starting with Model 1 (top row), the emitted intensity I_{em} reaches its maximum at the r_{isco} and then decays rapidly with increasing radius, with the peak shifting outward as the DM parameter b increases. The corresponding observed intensities (middle column) show that the Bardeen BH (black curve) produces three peaks: a dominant one from direct emission and two much smaller peaks associated with the lensing and photon ring contributions. For the PFDM-Bardeen BHs (green and red curves), only two peaks remain, since the photon ring contribution is almost entirely suppressed; the primary peak again originates from direct emission. Increasing b reduces the overall intensity amplitude. The rightmost column, which combines the images for different values of b , demonstrates that the DM parameter significantly modifies the resulting brightness distribution.

In Model 2 (middle row), the emission profile again shifts outward as the DM parameter b increases. Yet the corresponding observed intensity displays only two peaks—arising from the direct emission and the lensing ring—for both the Bardeen and PFDM-Bardeen BHs. The Bardeen case remains the brightest, while the presence of DM consistently reduces the overall luminosity. Furthermore, the model 3 (bottom row) yields an analogous behavior: the observed flux is dominated entirely by the direct emission, with contributions from the lensing and photon rings effectively absent. Overall, these results demonstrate that the DM parameter b exerts a clear suppressive effect on the observed brightness. The sensitivity of the intensity distribution to b underscores that thin disk optical signatures provide an effective diagnostic of the DM environment surrounding BHs.

Figure 8 examines the influence of magnetic charge $g/M = 0, 0.15, 0.3$ while keeping the DM parameter fixed at $b/M = 0.1$. Overall, the magnetic charge produces only minor modifications to the emitted intensity, the observed intensity, and the resulting optical appearance. In Model 1, both the PFDM-Sch and PFDM-Bardeen BHs exhibit only two peaks dominated by the direct emission with the PFDM-Sch case showing a slightly higher brightness than its Bardeen counterpart. Model 2 leads to the same qualitative behavior. Model 3, however, reveals a notable distinction: the PFDM-Sch BH displays three peaks, with the latter two being small but still discernible in the optical appearance, whereas the PFDM-Bardeen BHs lacks these additional features entirely. This implies that, provided

sufficient observational resolution, the faint secondary peaks associated with Model 3 could serve as a diagnostic of the magnetic charge. In this sense, Model 3 offers a potentially viable method for probing the presence of a magnetic charge in PFDM-Bardeen BH.

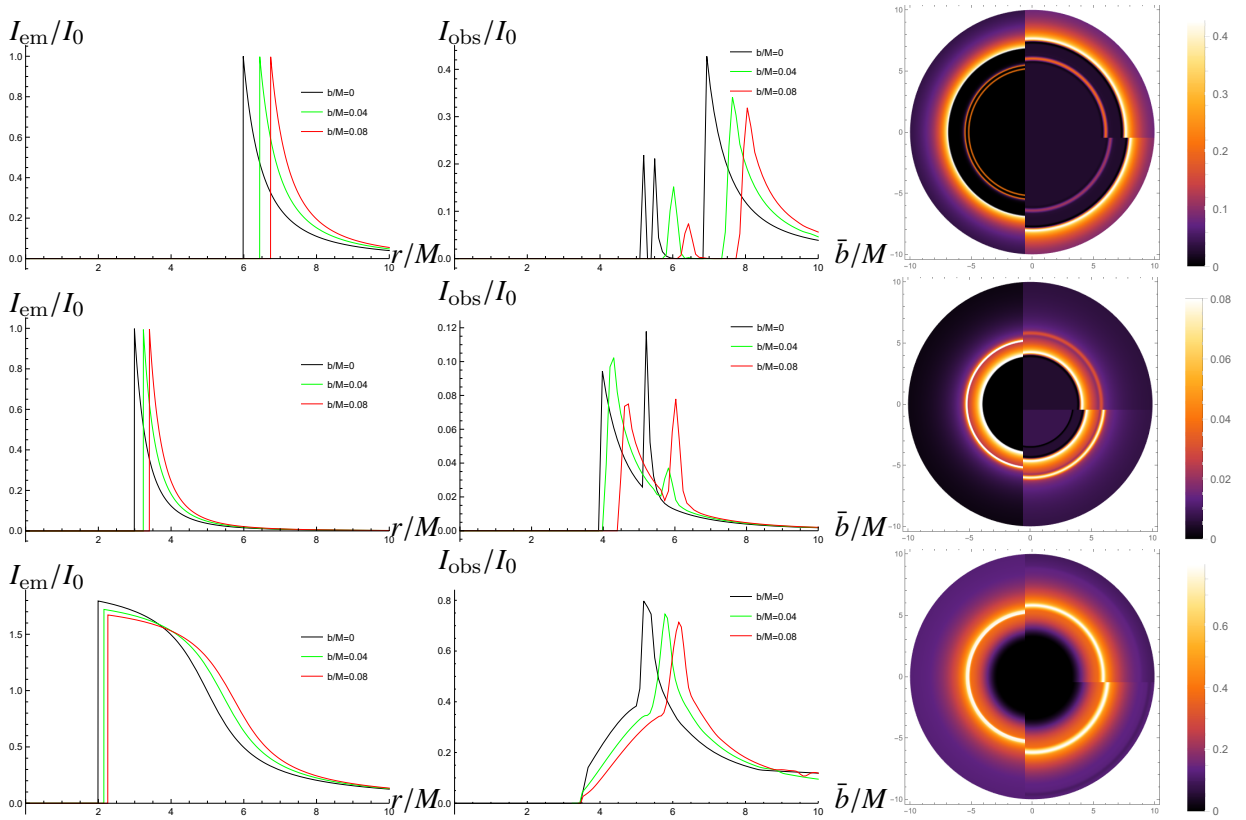


FIG. 7: The face-on optical appearance of the thin disk is displayed for three distinct emission prescriptions. The top, middle, and bottom rows correspond to Models 1, 2, and 3, respectively. In each row, the black, green, and red images represent configurations with fixed magnetic charge $g/M = 0.1$ and DM parameters $b/M = 0, 0.04$ and 0.08 . For all panels, both the emitted intensity I_{em} and the observed intensity I_{obs} are rescaled by the maximum emission I_0 outside the event horizon, ensuring a uniform normalization across models and parameter choices.

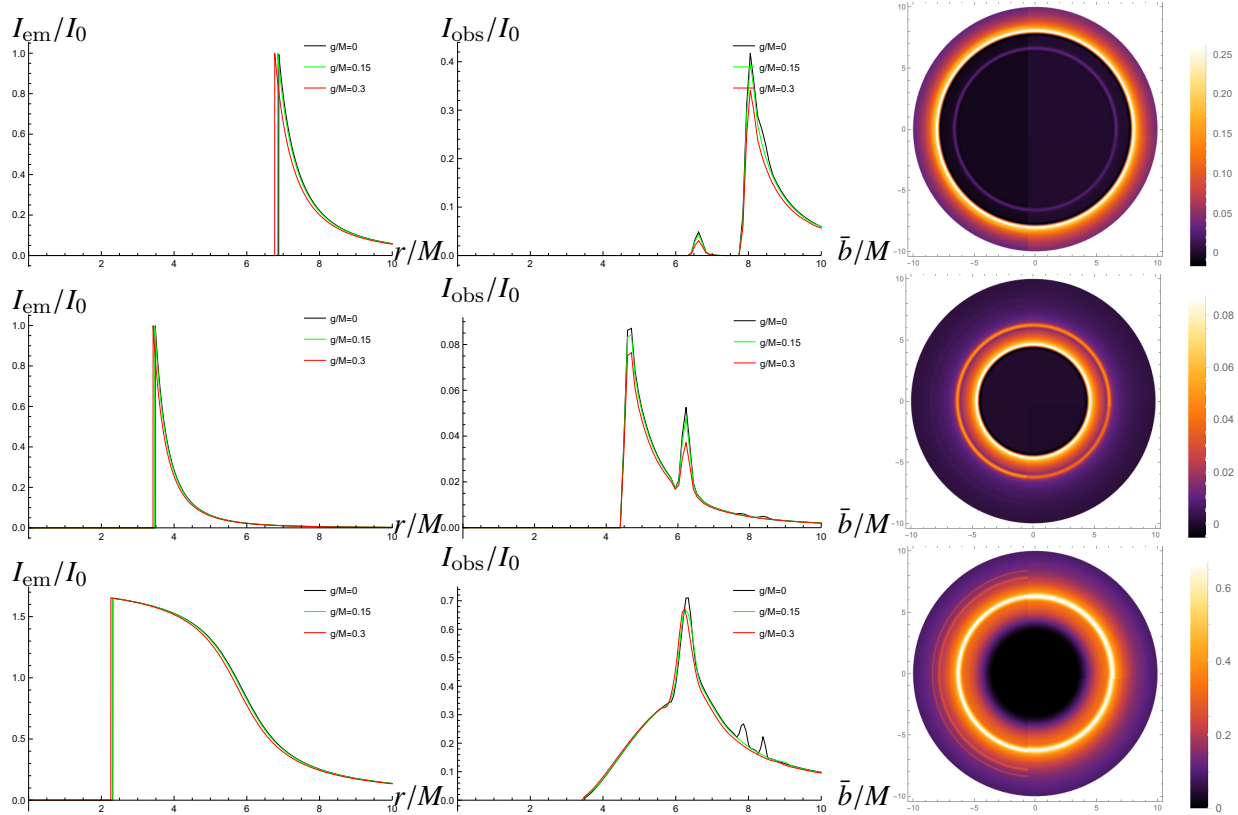


FIG. 8: In each row, the black, green, and red panels correspond to configurations with a fixed DM parameter $b/M = 0.1$ and magnetic charges $g/M = 0, 0.15$, and 0.30 , respectively. For the intensity calculations, we adopt the corresponding $r_{\text{isco}}/M = 6.87751, 6.85051$, and 6.76815 . The optical appearances obtained for these three parameter choices are then assembled into a composite image, shown in the rightmost column.

V. PRIMARY AND SECONDARY IMAGING FEATURES OF THIN ACCRETION DISKS

In this chapter, we investigate the imaging properties of thin accretion disks by systematically analyzing both the first-order (primary) and second-order (secondary) emission. These two levels of imaging encode distinct aspects of photon trajectories in curved spacetime: the primary image is dominated by direct photons reaching the observer with minimal deflection, while the secondary image arises from strongly lensed photons that execute additional orbits around BH. By comparing these structures across different parameter choices—such as the magnetic charge g , DM parameter b , we aim to clarify how the underlying BH shapes the optical appearance of the disk. This analysis provides a refined diagnostic framework

for identifying subtle signatures of modified gravity or matter-field effects in high-resolution BHs imaging.

A. Observation coordinate system

The imaging properties of a geometrically thin accretion disk can be examined by introducing an observer-adapted coordinate system, as shown in Fig. 9. In the BH's spherical coordinates (r, θ, ϕ) , the observer is positioned at $(\infty, \theta, 0)$, with the origin located at the BH center ($r = 0$). Within this observational frame $X'OY'$, consider an image point $q(\bar{b}, \alpha)$, characterized by the photon's impact parameter and its apparent angle α on the observer's sky. Extending the associated light ray backward along its geodesic leads to an intersection with the accretion disk at point $Q(r, \pi/2, \phi)$. By invoking the reversibility of null geodesics, any photon emitted from the disk at $Q(r, \pi/2, \phi)$ will traverse the same trajectory forward in time and arrive at the observer as the image point $q(\bar{b}, \alpha)$. This one-to-one correspondence between disk emission points and image coordinates provides the foundation for analyzing both primary and higher-order images.

Fixing the radial coordinate defines a family of photon trajectories that map onto a closed curve of constant radius on the observer's image plane. As illustrated on the Fig. 9, an orbit of fixed r in the equatorial plane intersects any plane spanned by angles α and $\alpha + \pi$ at two distinct points, separated by an azimuthal shift of π . For convenience, the directions $\alpha = 0$ and $\phi = 0$ are aligned with the X' -axis of the observer and the X -axis of the BH coordinate system, respectively.

From simple spatial geometry, one can determine the angle φ between the rotation axis and the line segment (OQ), which connects the observer to the emission point on the orbit. Geometrically, the angle φ can be expressed as [18, 52, 117]

$$\varphi = \frac{\pi}{2} + \arctan(\tan \theta \sin \alpha). \quad (25)$$

As the parameter \bar{b} approaches the critical value \bar{b}_c , photons experience increasingly pronounced gravitational deflection, allowing a single emission point Q on the disk to generate multiple distinct image locations in the observer's sky. These image locations are indexed by ordering their azimuthal deflections, so that q^n ($n \in \mathbb{N}$) designates the image produced after the n -th accumulated winding, with n representing the image order.

In the $X'OY'$ plane, all even-order images are projected onto the same side as the emission direction α , whereas odd-order images are reflected to the opposite side, appearing around $\alpha + \pi$. The cumulative azimuthal shift that gives rise to the n -th image is denoted by φ^n , defined as

$$\varphi^n = \begin{cases} n\pi + (-1)^n \left[\frac{\pi}{2} + \arctan(\tan \theta \sin \alpha) \right] & , n \in \text{even} \\ (n+1)\pi + (-1)^n \left[\frac{\pi}{2} + \arctan(\tan \theta \sin \alpha) \right] & , n \in \text{odd} \end{cases} \quad (26)$$

When $n = 0$, the image corresponds to the observer's direct view of the disk—its primary appearance without any additional winding of the photon trajectory. Increasing n to 1, 2, 3, and beyond designates progressively higher-order images, each arising from photons that have undergone additional azimuthal winding before reaching the observer, thereby producing secondary, tertiary, and subsequent visual repetitions of the emitting region. In the following subsection, we provide a detailed examination of the primary and secondary images produced by the PFDM–Bardeen BH, emphasizing how variations in the model parameters and the observer's viewing angle modulate the resulting imaging features.

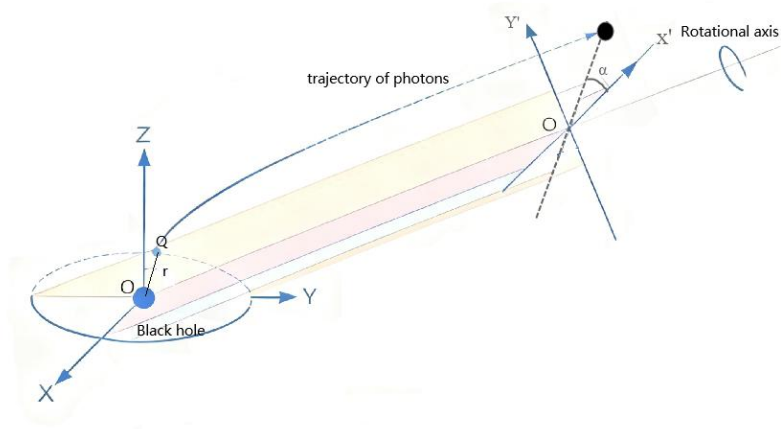


FIG. 9: The XYZ coordinate system is embedded in the BH. A photon emitted from a radius r propagates toward the observer's coordinate system $X'OY'$, forming an angle α in the observer's frame. The black point corresponds to the coordinate $q(\bar{b}, \alpha)$.

B. Investigation of direct and secondary images

Photons arriving from large distances follow trajectories determined by their impact parameter. As each photon approaches PFDM-Bardeen BH, its path is progressively bent by the gravitational field, and the total angular deviation accumulated by the time it reaches its point of closest approach r_{\min} is encoded in the function $\varphi_1(\bar{b})$. This curve serves as a reference: trajectories that accumulate less angular advance than $\varphi_1(\bar{b})$ form the family we denote by $\varphi_2(\bar{b})$, whereas those undergoing greater angular advance constitute the branch $\varphi_3(\bar{b})$. Accordingly, the quantities may be defined as

$$\begin{cases} \varphi_1(\bar{b}) = \int_0^{u_{\min}} \frac{1}{\sqrt{G(u)}} du, \\ \varphi_2(\bar{b}) = \int_0^{u_r} \frac{1}{\sqrt{G(u)}} du, \\ \varphi_3(\bar{b}) = 2 \int_0^{u_{\min}} \frac{1}{\sqrt{G(u)}} du - \int_0^{u_r} \frac{1}{\sqrt{G(u)}} du. \end{cases} \quad (27)$$

Using Eq. (27), we numerically integrate the photon trajectories and obtain the dependence of $\varphi(\bar{b})$ on the impact parameter \bar{b} for the PFDM-Bardeen BH, evaluated at fixed radius r with parameters $g/M = b/M = 0.1$. As illustrated in Fig. 10, the pink dashed curve represents the constant- r contour associated with the critical impact parameter \bar{b}_c , while the purple dashed curve shows the dependence of φ on \bar{b} evaluated at the photon's point of closest approach to the BH. The contour curves become increasingly convex as the radius r grows, and their intersections with the purple curve identify the corresponding values of φ at these turning points. Using this family of contours curves, we reconstruct the primary and secondary images of the accretion disk, as presented in Fig. 11.

The first two rows of Fig. 11 display the primary and secondary images of the accretion disk for a fixed magnetic charge $g/M = 0.1$, viewed at inclination angles $\theta = 0^\circ$, 40° , and 80° . The primary images are significantly sharper and more distinct than the secondary ones, and as the viewing angle increases, the contours gradually evolve into the characteristic appearance of thin accretion disk. In each panel, the cases $b/M = 0$, 0.04 , and 0.08 are juxtaposed, revealing that larger values of b systematically enlarge the resulting image contours. This dependence on the DM parameter becomes even more pronounced in the secondary images, where its influence is markedly stronger.

The third and fourth rows present the evolution of the image contours as the viewing

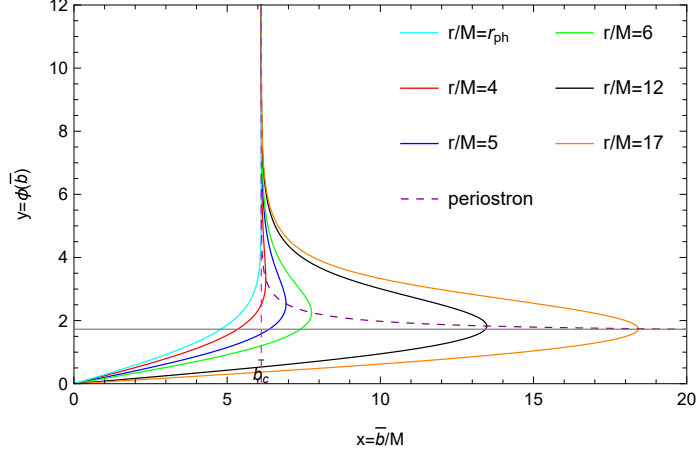


FIG. 10: The deflection $\varphi(b)$ is shown for various orbital radii r , illustrating how the bending angle associated with each intersection point evolves as a function of the impact parameter \bar{b} .

inclination varies, with the DM parameter fixed at $b/M = 0.01$. Each panel combines the three magnetic charge configurations $g/M = 0, 0.15$, and 0.3 . The contour morphology changes appreciably with the observer's angle; however, the influence of the magnetic charge is negligible—its impact on both the primary and secondary images is practically indistinguishable. This implies that any observational discrimination of a PFDM–Bardeen BH must primarily rely on the value of the DM parameter b . The presence of DM produces a clear enlargement of the accretion disk image.

C. Radiative intensity profile of accretion Disk

In this subsection, we analyze the radial distribution of the observed radiative flux emitted by the accretion disk within the Novikov–Thorne framework. The model is based on three essential assumptions (1): The accretion flow is a geometrically thin, optically thick disk in a steady state with a constant mass accretion rate. The gas follows nearly Keplerian circular orbits between the r_{isco} and outer radius r_{out} , with the disk lying on the equatorial plane and aligned with the BH spin axis. The self-gravity of the disk is negligible. (2): The dissipated energy is efficiently converted into radiation, allowing the disk to emit locally as a blackbody in thermal equilibrium. The emergent flux is perpendicular to the disk surface, and the continuum spectrum is dominated by thermal emission. (3): The underlying geometry is

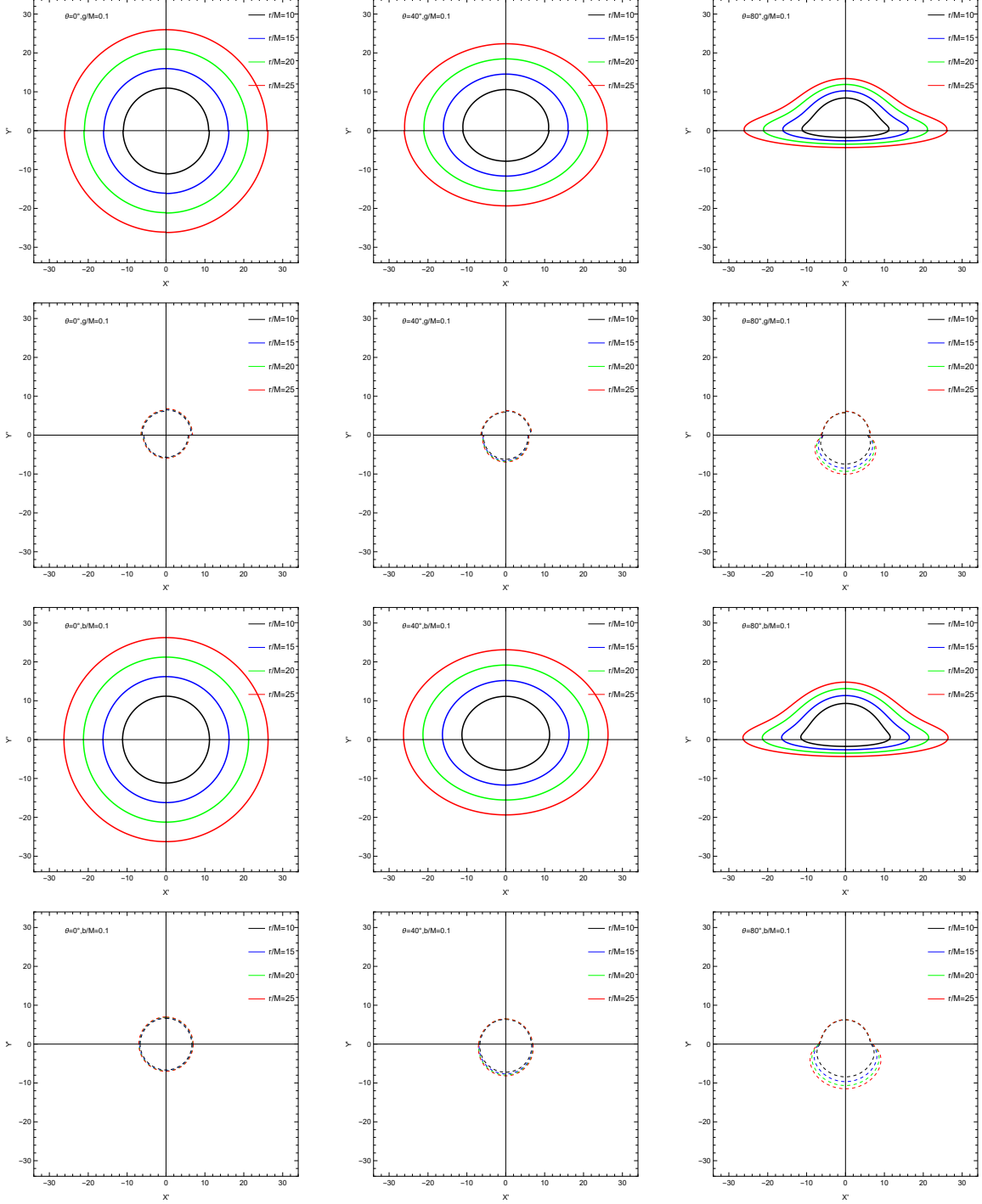


FIG. 11: The top two rows display the primary and secondary images for fixed $g/M = 0.1$ at viewing angles $\theta = 0^\circ, 40^\circ, 80^\circ$. In each panel, the cases $b/M = 0, 0.04, 0.08$ are combined into a single composite image for direct comparison. The bottom two rows show the corresponding primary and secondary images obtained by fixing $b/M = 0.1$ and varying the viewing angle over the same set ($0^\circ, 40^\circ, 80^\circ$). Here, the configurations with $g/M = 0, 0.15, 0.3$ are merged into each panel, enabling a unified assessment of how the magnetic charge influences the imaging structure.

stationary, axisymmetric, asymptotically flat, and symmetric with respect to the equatorial plane, ensuring that the particle motion and emitted radiation are governed solely by the background metric.

The radiative energy flux $F(r)$ can be defined as

$$F(r) = -\frac{\dot{M}}{4\pi\sqrt{-g}}\frac{\Omega_{,r}}{(\tilde{E}-\Omega\tilde{L})^2}\int_{r_{\text{isco}}}^r(\tilde{E}-\Omega\tilde{L})\tilde{L}_{,r}\mathrm{d}r. \quad (28)$$

This expression is commonly adopted in the literature and is applicable specifically within cylindrical coordinates. When rewritten in spherical coordinates and with physical dimensions reinstated, it takes the following form [118]

$$F(r) = -\frac{c^2\dot{M}}{4\pi\sqrt{-g/g_{\theta\theta}}}\frac{\Omega_{,r}}{(\tilde{E}-\Omega\tilde{L})^2}\int_{r_{\text{isco}}}^r(\tilde{E}-\Omega\tilde{L})\tilde{L}_{,r}\mathrm{d}r, \quad (29)$$

where c denotes the speed of light. Subsequently, we consider accretion onto BH of mass $M = 2 \times 10^6 M_\odot$, assuming the accretion rate $\dot{M} = 2 \times 10^{-6} M_\odot \text{yr}^{-1}$. In addition, \tilde{E} , \tilde{L} , and Ω denote the specific energy, specific angular momentum, and angular velocity of test particle, respectively. Their explicit definitions can be found in our previous work [18, 19, 52, 119, 120].

Owing to the distinct gravitational environments at the disk and the observer, together with their relative motion, the emitted photons undergo a corresponding frequency shift. Consequently, the radiation flux measured by the observer is given by [29, 121]

$$F_{\text{obs}} = \frac{F(r)}{(1+z)^4}, \quad (30)$$

where z denotes the redshift accumulated by photons as they propagate from the disk to the distant observer. The corresponding factor $1+z$ incorporates the gravitational redshift produced by the spacetime curvature. Its explicit form is [117]

$$1+z = \frac{1+\Omega\bar{b}\sin\theta\cos\alpha}{\sqrt{-g_{tt}-\Omega^2g_{\phi\phi}}}. \quad (31)$$

Figures 12 and 13 present the primary and secondary images associated with the optical appearance of accretion disk surrounding the PFDM–Bardeen BH. In these panels, the observed radiation flux F_{obs} is color-mapped, where brighter, yellowish regions indicate higher flux, while the black background corresponds to vanishing emission. A well defined disk outline emerges when the viewing angle approaches 90° , whereas the morphology becomes

nearly circular as the inclination tends toward 0° . Moreover, when the model parameters are held fixed, the individual effects of g and b are not directly visible in the composite images. Their influence, however, has already been clearly demonstrated in the previous subsection. To further examine these effects, we compute the spatial distribution of the redshift z across the accretion disk images. As shown in Figures 14 and 15, the primary and secondary images are displayed together, with larger values of z corresponding to regions rendered in deeper red tones. Notably, this BH exhibits no observable blueshift ($z < 0$); all images show exclusively redshifted emission. This property may serve as a potential observational discriminator, since certain BHs do permit blueshifted regions.

VI. CONCLUSION

The study begins by examining the spacetime structure of PFDM-Bardeen BH. This analysis identifies the parameter ranges that ensure the existence of regular horizons and clarifies how the DM parameter and magnetic charge reshape the underlying geometry. Building on this foundation, observational constraints derived from the EHT are applied to the model. The comparison with M87* data yields a narrow viable interval for the DM parameter, restricted to $\mathcal{O}(10^{-1} - 10^{-2})$, while the magnetic charge introduces only subdominant modifications. These constraints significantly limit the physically relevant parameter space. Subsequently, we investigated photon dynamics around the BH, where null trajectories are classified into direct, lensing, and photon ring branches. The results show that the DM parameter has a pronounced effect on the photon sphere, shadow radius, transfer function, and intensity profiles generally enlarging the shadow and suppressing the observed flux. In contrast, variations in g produce only minor corrections across all observables.

The final part of the analysis explores the imaging of thin accretion disks, including primary and secondary images, radiative flux distributions, and redshift maps. The morphology of the disk images is strongly influenced by the viewing inclination, with edge-on perspectives revealing distinct disk contours. Consistent with earlier findings, the DM parameter substantially alters image size and brightness, whereas the magnetic charge plays a negligible role. Notably, all images exhibit purely redshifted emission, providing an additional observational signature that may help distinguish PFDM-Bardeen BH from other

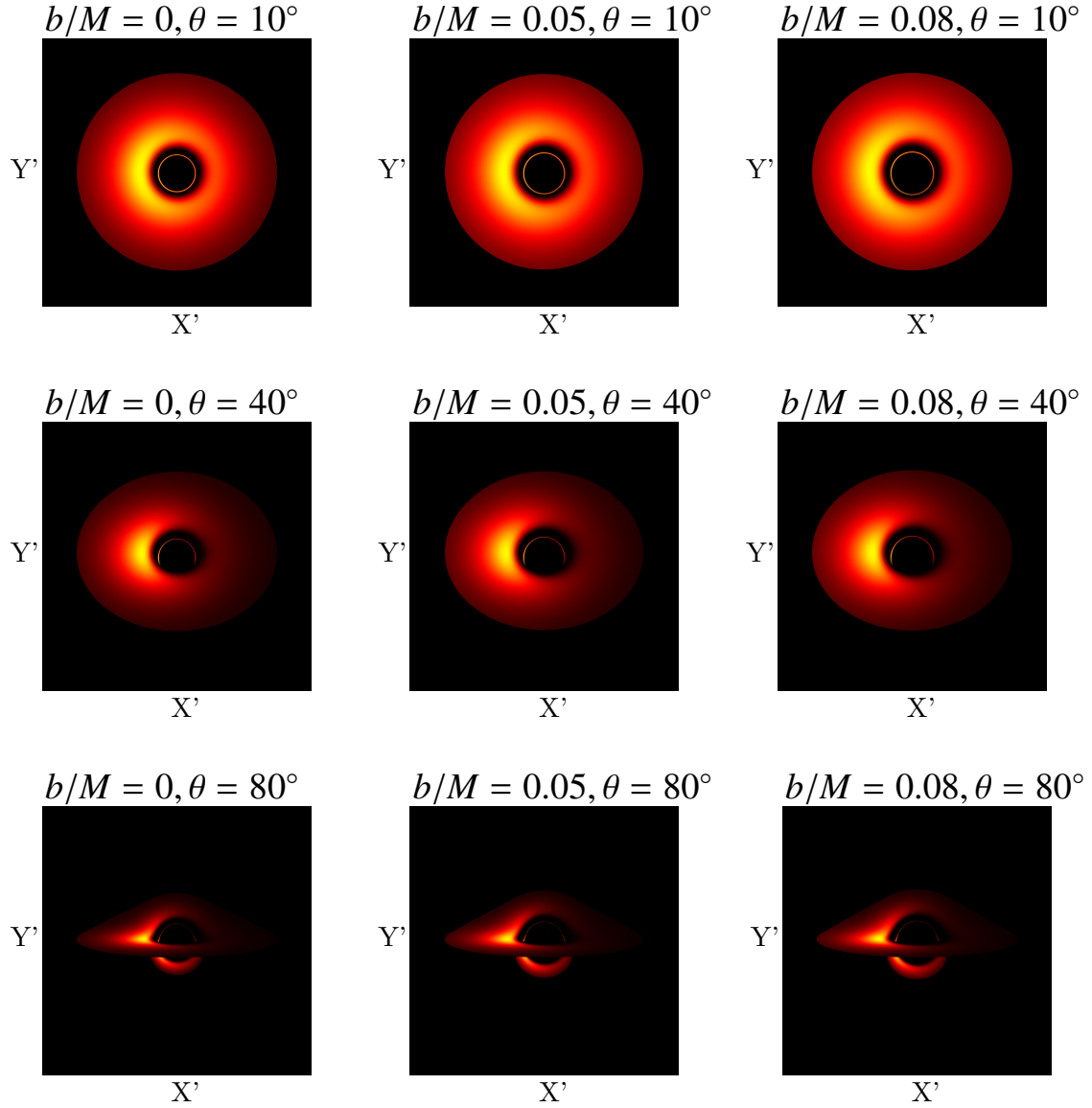


FIG. 12: This figure presents the distribution of F_{obs} , with the primary and secondary images combined. It illustrates the cases for fixed magnetic charge $g/M = 0.1$, considering viewing angles of 10° , 40° , and 80° , and comparing the DM parameters $b/M = 0$, 0.05 , and 0.08 .

compact objects.

Overall, the results demonstrate that DM exerts the dominant influence on both shadow geometry and optical appearance, while magnetic charge contributes only marginal effects. These conclusions highlight the potential of high-resolution BH imaging to probe the interplay between regular BHs and their surrounding DM environments.

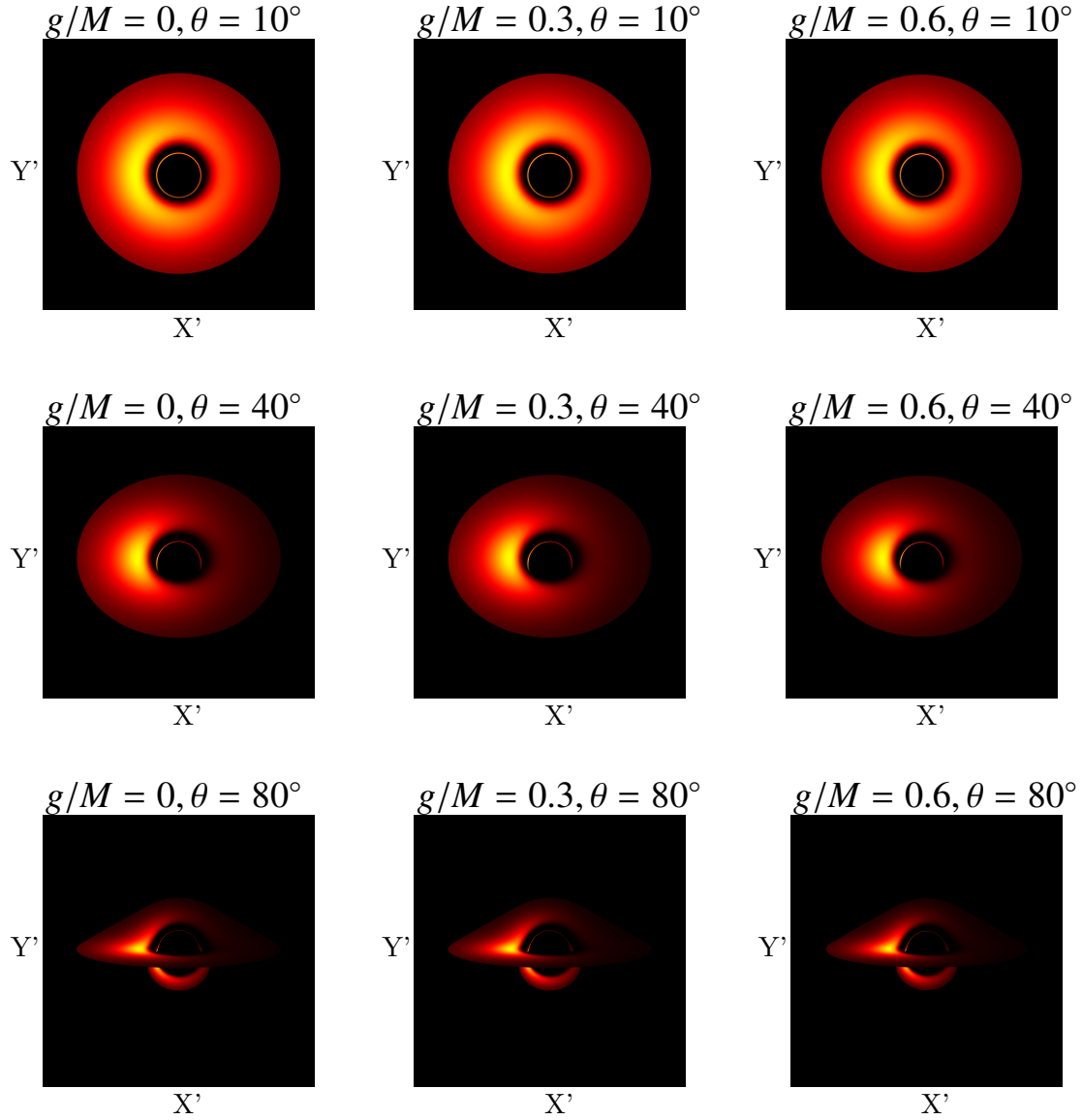


FIG. 13: The figure shows the cases with fixed DM parameter $b/M = 0.1$, for viewing angles of 10° , 40° , and 80° , considering magnetic charges $g/M = 0$, 0.3 , and 0.6 .

ACKNOWLEDGMENTS

This study was supported by the National Natural Science Foundation of China (Grant Nos. 12333008 and 12305070) and the Basic Research Program of Shanxi Province (Grant No. 202303021222018).

-
- [1] Kazunori Akiyama et al. First M87 Event Horizon Telescope Results. I. The Shadow of the Supermassive Black Hole. *Astrophys. J. Lett.*, 875:L1, 2019.

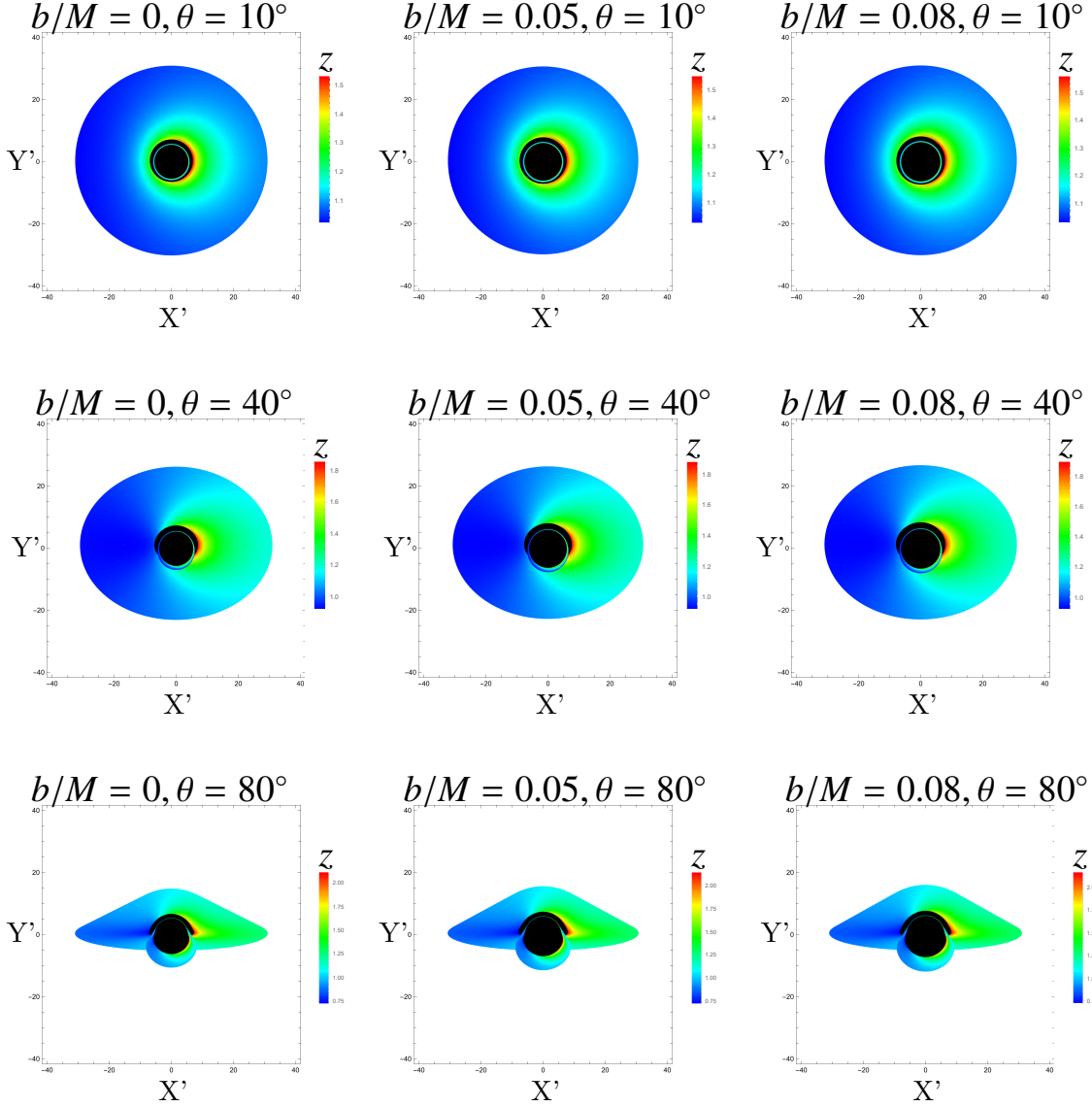


FIG. 14: This figure illustrates the distribution of the redshift z across the accretion disk for different viewing angles. The magnitude of the redshift is indicated by the color bar on the right. As before, we fix $g/M = 0.1$ and examine how variations in the DM parameter b modify the disk appearance under different observational inclinations.

- [2] Kazunori Akiyama et al. First M87 Event Horizon Telescope Results. II. Array and Instrumentation. *Astrophys. J. Lett.*, 875(1):L2, 2019.
- [3] Kazunori Akiyama et al. First M87 Event Horizon Telescope Results. III. Data Processing and Calibration. *Astrophys. J. Lett.*, 875(1):L3, 2019.
- [4] Kazunori Akiyama et al. First M87 Event Horizon Telescope Results. IV. Imaging the Central Supermassive Black Hole. *Astrophys. J. Lett.*, 875(1):L4, 2019.

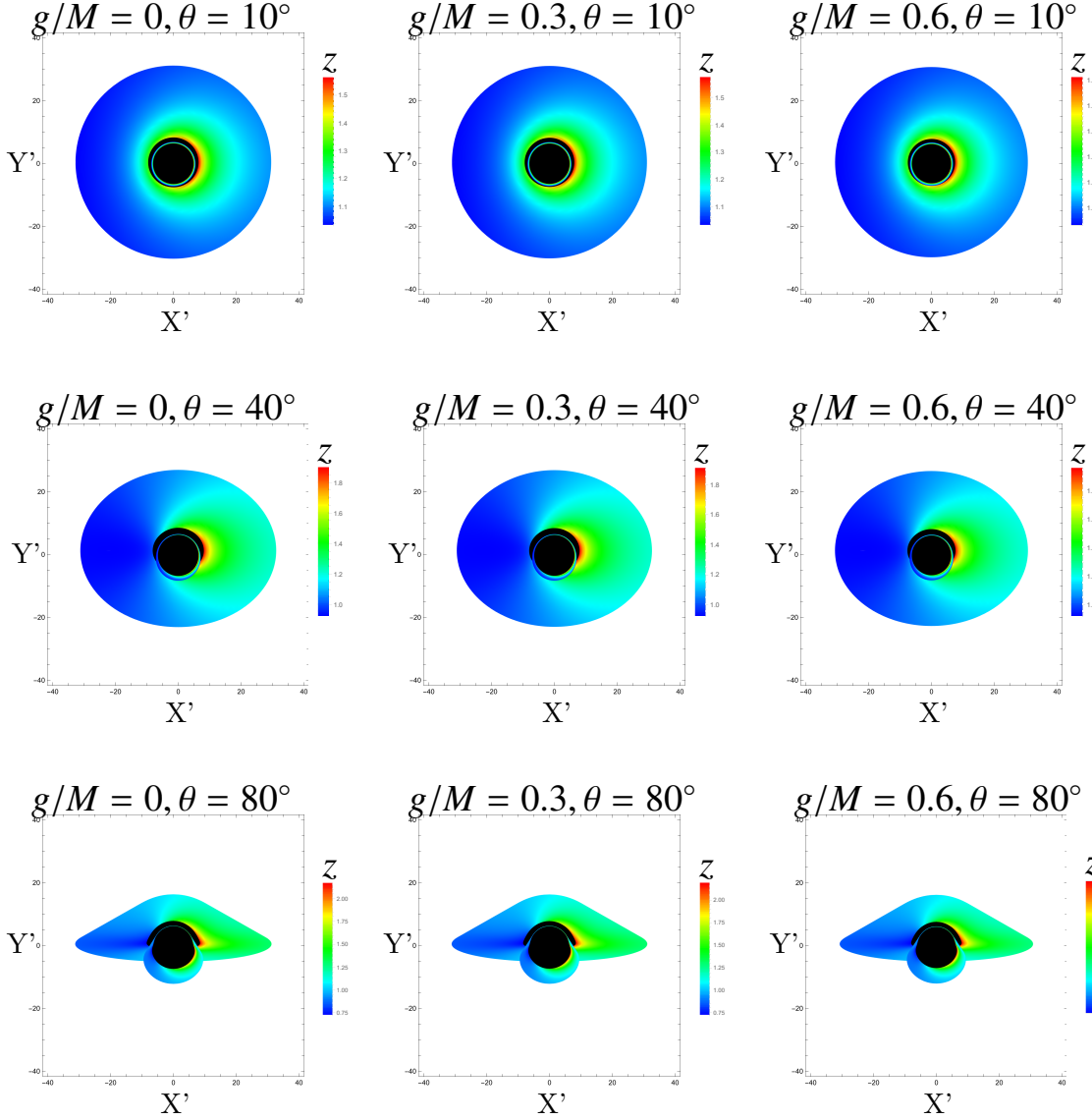


FIG. 15: Three representative viewing angles are fixed together with $b/M = 0.1$, allowing us to examine how variations in the magnetic charge g/M influence the morphology of both the primary and secondary images.

- [5] Kazunori Akiyama et al. First M87 Event Horizon Telescope Results. V. Physical Origin of the Asymmetric Ring. *Astrophys. J. Lett.*, 875(1):L5, 2019.
- [6] Kazunori Akiyama et al. First M87 Event Horizon Telescope Results. VI. The Shadow and Mass of the Central Black Hole. *Astrophys. J. Lett.*, 875(1):L6, 2019.
- [7] Haroldo C. D. Lima, Junior., Luís C. B. Crispino, Pedro V. P. Cunha, and Carlos A. R. Herdeiro. Can different black holes cast the same shadow? *Phys. Rev. D*, 103(8):084040, 2021.

- [8] Sebastian H. Völkel, Enrico Barausse, Nicola Franchini, and Avery E. Broderick. EHT tests of the strong-field regime of general relativity. *Class. Quant. Grav.*, 38(21):21LT01, 2021.
- [9] Misba Afrin, Rahul Kumar, and Sushant G. Ghosh. Parameter estimation of hairy Kerr black holes from its shadow and constraints from M87*. *Mon. Not. Roy. Astron. Soc.*, 504(4):5927–5940, 2021.
- [10] Merce Guerrero, Gonzalo J. Olmo, Diego Rubiera-Garcia, and Diego Sáez-Chillón Gómez. Shadows and optical appearance of black bounces illuminated by a thin accretion disk. *JCAP*, 08:036, 2021.
- [11] Javier Badía and Ernesto F. Eiroa. Influence of an anisotropic matter field on the shadow of a rotating black hole. *Phys. Rev. D*, 102(2):024066, 2020.
- [12] Pedro V. P. Cunha, Carlos A. R. Herdeiro, and Eugen Radu. EHT constraint on the ultralight scalar hair of the M87 supermassive black hole. *Universe*, 5(12):220, 2019.
- [13] Naoki Tsukamoto. Black hole shadow in an asymptotically-flat, stationary, and axisymmetric spacetime: The Kerr-Newman and rotating regular black holes. *Phys. Rev. D*, 97(6):064021, 2018.
- [14] Pedro V. P. Cunha, Emanuele Berti, and Carlos A. R. Herdeiro. Light-Ring Stability for Ultracompact Objects. *Phys. Rev. Lett.*, 119(25):251102, 2017.
- [15] P. V. P. Cunha, J. Grover, C. Herdeiro, E. Radu, H. Runarsson, and A. Wittig. Chaotic lensing around boson stars and Kerr black holes with scalar hair. *Phys. Rev. D*, 94(10):104023, 2016.
- [16] Ahmadjon Abdujabbarov, Muhammed Amir, Bobomurat Ahmedov, and Sushant G. Ghosh. Shadow of rotating regular black holes. *Phys. Rev. D*, 93(10):104004, 2016.
- [17] Yingdong Wu, Ziqiang Cai, Zhenglong Ban, Haiyuan Feng, and Wei-Qiang Chen. Probing Einstein–Maxwell-scalar black hole via thin accretion disks and shadows with EHT observations of M87* and Sgr A*. *Eur. Phys. J. C*, 85(9):1085, 2025.
- [18] Ziqiang Cai, Zhenglong Ban, Lu Wang, Haiyuan Feng, and Zheng-Wen Long. Thin accretion disk around Schwarzschild-like black hole in bumblebee gravity. *JCAP*, 10:101, 2025.
- [19] Haiyuan Feng, Rong-Jia Yang, and Wei-Qiang Chen. Thin accretion disk and shadow of Kerr–Sen black hole in Einstein–Maxwell-dilaton–axion gravity. *Astropart. Phys.*, 166:103075, 2025.
- [20] Ailin Liu, Tong-Yu He, Ming Liu, Zhan-Wen Han, and Rong-Jia Yang. Possible signatures of

- higher dimension in thin accretion disk around brane world black hole. JCAP, 07:062, 2024.
- [21] Kazunori Akiyama et al. First Sagittarius A* Event Horizon Telescope Results. I. The Shadow of the Supermassive Black Hole in the Center of the Milky Way. *Astrophys. J. Lett.*, 930(2):L12, 2022.
 - [22] Kazunori Akiyama et al. First Sagittarius A* Event Horizon Telescope Results. II. EHT and Multiwavelength Observations, Data Processing, and Calibration. *Astrophys. J. Lett.*, 930(2):L13, 2022.
 - [23] Kazunori Akiyama et al. First Sagittarius A* Event Horizon Telescope Results. III. Imaging of the Galactic Center Supermassive Black Hole. *Astrophys. J. Lett.*, 930(2):L14, 2022.
 - [24] Kazunori Akiyama et al. First Sagittarius A* Event Horizon Telescope Results. IV. Variability, Morphology, and Black Hole Mass. *Astrophys. J. Lett.*, 930(2):L15, 2022.
 - [25] Kazunori Akiyama et al. First Sagittarius A* Event Horizon Telescope Results. V. Testing Astrophysical Models of the Galactic Center Black Hole. *Astrophys. J. Lett.*, 930(2):L16, 2022.
 - [26] Kazunori Akiyama et al. First Sagittarius A* Event Horizon Telescope Results. VI. Testing the Black Hole Metric. *Astrophys. J. Lett.*, 930(2):L17, 2022.
 - [27] Carlos A. R. Herdeiro. Black Holes: On the Universality of the Kerr Hypothesis. *Lect. Notes Phys.*, 1017:315–331, 2023.
 - [28] J. L. Synge. The Escape of Photons from Gravitationally Intense Stars. *Mon. Not. Roy. Astron. Soc.*, 131(3):463–466, 1966.
 - [29] J. P. Luminet. Image of a spherical black hole with thin accretion disk. *Astron. Astrophys.*, 75:228–235, 1979.
 - [30] Kenta Hioki and Kei-ichi Maeda. Measurement of the Kerr Spin Parameter by Observation of a Compact Object’s Shadow. *Phys. Rev. D*, 80:024042, 2009.
 - [31] J. M. Bardeen. Timelike and null geodesics in the Kerr metric. *Proceedings, Ecole d’Eté de Physique Théorique: Les Astres Occlus : Les Houches, France, August, 1972*, 215–240, pages 215–240, 1973.
 - [32] Zdenek Stuchlík and Jan Schee. Shadow of the regular Bardeen black holes and comparison of the motion of photons and neutrinos. *Eur. Phys. J. C*, 79(1):44, 2019.
 - [33] Akifumi Yumoto, Daisuke Nitta, Takeshi Chiba, and Naoshi Sugiyama. Shadows of Multi-Black Holes: Analytic Exploration. *Phys. Rev. D*, 86:103001, 2012.

- [34] Ahmadjon Abdujabbarov, Muhammed Amir, Bobomurat Ahmedov, and Sushant G. Ghosh. Shadow of rotating regular black holes. *Phys. Rev. D*, 93(10):104004, 2016.
- [35] Muhammed Amir and Sushant G. Ghosh. Shapes of rotating nonsingular black hole shadows. *Phys. Rev. D*, 94(2):024054, 2016.
- [36] M. Sharif and Sehrish Iftikhar. Shadow of a Charged Rotating Non-Commutative Black Hole. *Eur. Phys. J. C*, 76(11):630, 2016.
- [37] Shao-Wen Wei and Yu-Xiao Liu. Observing the shadow of Einstein-Maxwell-Dilaton-Axion black hole. *JCAP*, 11:063, 2013.
- [38] Ahmadjon Abdujabbarov, Farruh Atamurotov, Yusuf Kucukakca, Bobomurat Ahmedov, and Ugur Camci. Shadow of Kerr-Taub-NUT black hole. *Astrophys. Space Sci.*, 344:429–435, 2013.
- [39] Juliano C. S. Neves. Constraining the tidal charge of brane black holes using their shadows. *Eur. Phys. J. C*, 80(8):717, 2020.
- [40] Leonardo Amarilla and Ernesto F. Eiroa. Shadow of a Kaluza-Klein rotating dilaton black hole. *Phys. Rev. D*, 87(4):044057, 2013.
- [41] Farruh Atamurotov, Ahmadjon Abdujabbarov, and Bobomurat Ahmedov. Shadow of rotating non-Kerr black hole. *Phys. Rev. D*, 88(6):064004, 2013.
- [42] Haryanto M. Siahaan. Black hole shadows in accelerating Kerr–Newman–Taub–NUT and Braneworld spacetimes. *Eur. Phys. J. C*, 85(4):431, 2025.
- [43] He-Bin Zheng, Meng-Qi Wu, Guo-Ping Li, and Qing-Quan Jiang. Shadows and accretion disk images of charged rotating black hole in modified gravity theory. *Eur. Phys. J. C*, 85(1):46, 2025.
- [44] Gaetano Lambiase, Dhruba Jyoti Gogoi, Reggie C. Pantig, and Ali Övgün. Shadow and quasinormal modes of the rotating Einstein–Euler–Heisenberg black holes. *Phys. Dark Univ.*, 48:101886, 2025.
- [45] Wentao Liu, Di Wu, and Jieci Wang. Shadow of slowly rotating Kalb-Ramond black holes. *JCAP*, 05:017, 2025.
- [46] Songbai Chen and Jiliang Jing. Kerr black hole shadows from axion-photon coupling. *JCAP*, 05:023, 2024.
- [47] Muhammad Zahid, Odil Yunusov, Chao Shen, Javlon Rayimbaev, and Sokhibjan Muminov. Shadows and quasinormal modes of rotating black holes in Horndeski theory: Parameter

- constraints using EHT observations of M87* and Sgr A*. *Phys. Dark Univ.*, 47:101734, 2025.
- [48] Xinyu Wang, Zhixing Zhao, Xiao-Xiong Zeng, and Xin-Yang Wang. Revisiting the shadow of Johannsen-Psaltis black holes. *Phys. Rev. D*, 111(8):084054, 2025.
 - [49] Chen-Yu Yang, M. Israr Aslam, Xiao-Xiong Zeng, and Rabia Saleem. Shadow images of Ghosh-Kumar rotating black hole illuminated by spherical light sources and thin accretion disks. *JHEAp*, 46:345, 2025.
 - [50] Mark Hindmarsh, Stephan J. Huber, Kari Rummukainen, and David J. Weir. Shape of the acoustic gravitational wave power spectrum from a first order phase transition. *Phys. Rev. D*, 96(10):103520, 2017. [Erratum: *Phys.Rev.D* 101, 089902 (2020)].
 - [51] Uma Papnoi, Farruh Atamurotov, Sushant G. Ghosh, and Bobomurat Ahmedov. Shadow of five-dimensional rotating Myers-Perry black hole. *Phys. Rev. D*, 90(2):024073, 2014.
 - [52] Ziqiang Cai, Zhenglong Ban, Lu Wang, Haiyuan Feng, and Zheng-Wen Long. Shadow and thin accretion disk around Ayón-Beato-García black hole coupled with cloud of strings. 6 2025.
 - [53] N. I. Shakura and R. A. Sunyaev. Black holes in binary systems. Observational appearance. *Astron. Astrophys.*, 24:337–355, 1973.
 - [54] Don N. Page and Kip S. Thorne. Disk-Accretion onto a Black Hole. Time-Averaged Structure of Accretion Disk. *Astrophys. J.*, 191:499–506, 1974.
 - [55] S. U. Viergutz. Image generation in Kerr geometry. I. Analytical investigations on the stationary emitter-observer problem. *American Academy of Pediatrics*, 272:355, May 1993.
 - [56] R. Speith, H. Riffert, and H. Ruder. The photon transfer function for accretion disks around a Kerr black hole. *Computer Physics Communications*, 88(2-3):109–120, August 1995.
 - [57] Claudio Fanton, Massimo Calvani, Fernando de Felice, and Andrej Cadez. Detecting Accretion Disks in Active Galactic Nuclei. *Publications of the Astronomical Society of Japan*, 49:159–169, April 1997.
 - [58] Avery E. Broderick and Abraham Loeb. Imaging bright spots in the accretion flow near the black hole horizon of Sgr A*. *Mon. Not. Roy. Astron. Soc.*, 363:353–362, 2005.
 - [59] Jason Dexter. A public code for general relativistic, polarised radiative transfer around spinning black holes. *Mon. Not. Roy. Astron. Soc.*, 462(1):115–136, 2016.
 - [60] F. H. Vincent, T. Paumard, E. Gourgoulhon, and G. Perrin. GYOTO: a new general rela-

- tivistic ray-tracing code. *Class. Quant. Grav.*, 28:225011, 2011.
- [61] Yehui Hou, Zhenyu Zhang, Haopeng Yan, Minyong Guo, and Bin Chen. Image of a Kerr-Melvin black hole with a thin accretion disk. *Phys. Rev. D*, 106(6):064058, 2022.
 - [62] Zhenyu Zhang, Yehui Hou, Minyong Guo, and Bin Chen. Imaging thick accretion disks and jets surrounding black holes. *JCAP*, 05:032, 2024.
 - [63] Galin Gylulchev, Petya Nedkova, Tsvetan Vetsov, and Stoytcho Yazadjiev. Image of the Janis-Newman-Winicour naked singularity with a thin accretion disk. *Phys. Rev. D*, 100(2):024055, 2019.
 - [64] Rajibul Shaikh and Pankaj S. Joshi. Can we distinguish black holes from naked singularities by the images of their accretion disks? *JCAP*, 10:064, 2019.
 - [65] Cosimo Bambi, Katherine Freese, Sunny Vagnozzi, and Luca Visinelli. Testing the rotational nature of the supermassive object M87* from the circularity and size of its first image. *Phys. Rev. D*, 100(4):044057, 2019.
 - [66] Tim Johannsen. Testing the No-Hair Theorem with Observations of Black Holes in the Electromagnetic Spectrum. *Class. Quant. Grav.*, 33(12):124001, 2016.
 - [67] Delilah E. A. Gates, Shahar Hadar, and Alexandru Lupasca. Maximum observable blueshift from circular equatorial kerr orbiters. *Phys. Rev. D*, 102:104041, Nov 2020.
 - [68] Mert Okayay and Ali Övgün. Nonlinear electrodynamics effects on the black hole shadow, deflection angle, quasinormal modes and greybody factors. *JCAP*, 01(01):009, 2022.
 - [69] J. P. Luminet. Image of a spherical black hole with thin accretion disk. *Astron. Astrophys.*, 75:228–235, 1979.
 - [70] Yutaka Hirai, Shinya Wanajo, and Takayuki R. Saitoh. Enrichment of Strontium in Dwarf Galaxies. *Astrophys. J.*, 885:33, 2019.
 - [71] Heino Falcke, Fulvio Melia, and Eric Agol. Viewing the Shadow of the Black Hole at the Galactic Center. *The Astrophysical Journal Letters*, 528(1):L13–L16, January 2000.
 - [72] Cosimo Bambi. Can the supermassive objects at the centers of galaxies be traversable wormholes? the first test of strong gravity for mm/sub-mm very long baseline interferometry facilities. *Phys. Rev. D*, 87:107501, May 2013.
 - [73] Xiao-Xiong Zeng, Hai-Qing Zhang, and Hongbao Zhang. Shadows and photon spheres with spherical accretions in the four-dimensional Gauss–Bonnet black hole. *Eur. Phys. J. C*, 80(9):872, 2020.

- [74] Sen Guo, Ke-Jian He, Guan-Ru Li, and Guo-Ping Li. The shadow and photon sphere of the charged black hole in Rastall gravity. *Class. Quant. Grav.*, 38(16):165013, 2021.
- [75] Xin Qin, Songbai Chen, and Jiliang Jing. Image of a regular phantom compact object and its luminosity under spherical accretions. *Class. Quant. Grav.*, 38(11):115008, 2021.
- [76] Samuel E. Gralla, Daniel E. Holz, and Robert M. Wald. Black Hole Shadows, Photon Rings, and Lensing Rings. *Phys. Rev. D*, 100(2):024018, 2019.
- [77] Gerard t Hooft and MJG1974AnIHP Veltman. One-loop divergencies in the theory of gravitation. In *Annales de l’IHP Physique théorique*, volume 20, pages 69–94, 1974.
- [78] Stanley Deser and P. van Nieuwenhuizen. One Loop Divergences of Quantized Einstein-Maxwell Fields. *Phys. Rev. D*, 10:401, 1974.
- [79] Stanley Deser, Hung-Sheng Tsao, and P. van Nieuwenhuizen. One Loop Divergences of the Einstein Yang-Mills System. *Phys. Rev. D*, 10:3337, 1974.
- [80] Stephen W. Hawking and George F. R. Ellis. *The Large Scale Structure of Space-Time*. Cambridge Monographs on Mathematical Physics. Cambridge University Press, 2 2023.
- [81] Gerard ’t Hooft and M. J. G. Veltman. One loop divergencies in the theory of gravitation. *Ann. Inst. H. Poincare A Phys. Theor.*, 20:69–94, 1974.
- [82] Guido Cognola, Ratbay Myrzakulov, Lorenzo Sebastiani, and Sergio Zerbini. Einstein gravity with Gauss-Bonnet entropic corrections. *Phys. Rev. D*, 88(2):024006, 2013.
- [83] Cong Zhang, Jerzy Lewandowski, Haida Li, and Yongge Ma. Bouncing evolution in a model of loop quantum gravity. *Phys. Rev. D*, 99(12):124012, 2019.
- [84] James Bardeen. Non-singular general relativistic gravitational collapse. In *Proceedings of the 5th International Conference on Gravitation and the Theory of Relativity*, page 87, September 1968.
- [85] Eloy Ayon-Beato and Alberto Garcia. The Bardeen model as a nonlinear magnetic monopole. *Phys. Lett. B*, 493:149–152, 2000.
- [86] Sean A. Hayward. Formation and evaporation of regular black holes. *Phys. Rev. Lett.*, 96:031103, 2006.
- [87] Eloy Ayon-Beato and Alberto Garcia. Regular black hole in general relativity coupled to nonlinear electrodynamics. *Phys. Rev. Lett.*, 80:5056–5059, 1998.
- [88] Waldemar Berej, Jerzy Matyjasek, Dariusz Tryniecki, and Mariusz Woronowicz. Regular black holes in quadratic gravity. *Gen. Rel. Grav.*, 38:885–906, 2006.

- [89] Yawar H. Khan, Sudhaker Upadhyay, and Prince A. Ganai. Stability of remnants of Bardeen regular black holes in presence of thermal fluctuations. *Mod. Phys. Lett. A*, 36(24):2130023, 2021.
- [90] Sharmanthie Fernando and Juan Correa. Quasinormal Modes of Bardeen Black Hole: Scalar Perturbations. *Phys. Rev. D*, 86:064039, 2012.
- [91] Hossein Ghaffarnejad and Hassan Niad. Weak Gravitational lensing from regular Bardeen black holes. *Int. J. Theor. Phys.*, 55(3):1492–1505, 2016.
- [92] Sheng Zhou, Juhua Chen, and Yongjiu Wang. Geodesic Structure of Test Particle in Bardeen Spacetime. *Int. J. Mod. Phys. D*, 21:1250077, 2012.
- [93] Yang Guo and Yan-Gang Miao. Weinhold geometry and thermodynamics of Bardeen AdS black holes. *Nucl. Phys. B*, 980:115839, 2022.
- [94] F. Zwicky. Die Rotverschiebung von extragalaktischen Nebeln. *Helvetica Physica Acta*, 6:110–127, January 1933.
- [95] V. C. Rubin, W. K. Ford, Jr., and N. Thonnard. Rotational properties of 21 SC galaxies with a large range of luminosities and radii, from NGC 4605 ($R=4\text{kpc}$) to UGC 2885 ($R=122\text{kpc}$). *The Astrophysical Journal*, 238:471–487, June 1980.
- [96] Erik Holmberg. A Study of Double and Multiple Galaxies Together with Inquiries into some General Metagalactic Problems. *Annals of the Observatory of Lund*, 6:1–173, January 1937.
- [97] Sinclair Smith. The Mass of the Virgo Cluster. *The Astrophysical Journal*, 83:23, January 1936.
- [98] P. A. R. Ade et al. Planck 2013 results. XVI. Cosmological parameters. *Astron. Astrophys.*, 571:A16, 2014.
- [99] Jamie Bamber, Katy Clough, Pedro G. Ferreira, Lam Hui, and Macarena Lagos. Growth of accretion driven scalar hair around kerr black holes. *Phys. Rev. D*, 103:044059, Feb 2021.
- [100] Katy Clough, Pedro G. Ferreira, and Macarena Lagos. Growth of massive scalar hair around a schwarzschild black hole. *Phys. Rev. D*, 100:063014, Sep 2019.
- [101] Vitor Cardoso, Kyriakos Destounis, Francisco Duque, Rodrigo Panosso Macedo, and Andrea Maselli. Gravitational waves from extreme-mass-ratio systems in astrophysical environments. *Phys. Rev. Lett.*, 129:241103, Dec 2022.
- [102] Arvind Borde. Regular black holes and topology change. *Phys. Rev. D*, 55:7615–7617, Jun 1997.

- [103] He-Xu Zhang, Yuan Chen, Tian-Chi Ma, Peng-Zhang He, and Jian-Bo Deng. Bardeen black hole surrounded by perfect fluid dark matter. *Chin. Phys. C*, 45(5):055103, 2021.
- [104] V. V. Kiselev. Quintessence and black holes. *Class. Quant. Grav.*, 20:1187–1198, 2003.
- [105] Ming-Hsun Li and Kwei-Chou Yang. Galactic Dark Matter in the Phantom Field. *Phys. Rev. D*, 86:123015, 2012.
- [106] Volker Perlick and Oleg Yu. Tsupko. Calculating black hole shadows: Review of analytical studies. *Phys. Rept.*, 947:1–39, 2022.
- [107] Volker Perlick, Oleg Yu. Tsupko, and Gennady S. Bisnovatyi-Kogan. Influence of a plasma on the shadow of a spherically symmetric black hole. *Phys. Rev. D*, 92(10):104031, 2015.
- [108] Yosuke Mizuno, Ziri Younsi, Christian M. Fromm, Oliver Porth, Mariafelicia De Laurentis, Hector Olivares, Heino Falcke, Michael Kramer, and Luciano Rezzolla. The Current Ability to Test Theories of Gravity with Black Hole Shadows. *Nature Astron.*, 2(7):585–590, 2018.
- [109] Prashant Kocherlakota et al. Constraints on black-hole charges with the 2017 EHT observations of M87*. *Phys. Rev. D*, 103(10):104047, 2021.
- [110] Sunny Vagnozzi et al. Horizon-scale tests of gravity theories and fundamental physics from the Event Horizon Telescope image of Sagittarius A. *Class. Quant. Grav.*, 40(16):165007, 2023.
- [111] Akhil Uniyal, Reggie C. Pantig, and Ali Övgün. Probing a non-linear electrodynamics black hole with thin accretion disk, shadow, and deflection angle with M87* and Sgr A* from EHT. *Phys. Dark Univ.*, 40:101178, 2023.
- [112] Jun Peng, Minyong Guo, and Xing-Hui Feng. Influence of quantum correction on black hole shadows, photon rings, and lensing rings. *Chin. Phys. C*, 45(8):085103, 2021.
- [113] Jinsong Yang, Cong Zhang, and Yongge Ma. Shadow and stability of quantum-corrected black holes. *Eur. Phys. J. C*, 83(7):619, 2023.
- [114] Samuel E. Gralla, Daniel E. Holz, and Robert M. Wald. Black Hole Shadows, Photon Rings, and Lensing Rings. *Phys. Rev. D*, 100(2):024018, 2019.
- [115] Xi-Jing Wang, Xiao-Mei Kuang, Yuan Meng, Bin Wang, and Jian-Pin Wu. Rings and images of Horndeski hairy black hole illuminated by various thin accretions. *Phys. Rev. D*, 107(12):124052, 2023.
- [116] Xiao-Xiong Zeng and Hai-Qing Zhang. Influence of quintessence dark energy on the shadow of black hole. *Eur. Phys. J. C*, 80(11):1058, 2020.

- [117] Lei You, Rui-bo Wang, Shi-Jie Ma, Jian-Bo Deng, and Xian-Ru Hu. Optical properties of Euler-Heisenberg black hole in the Cold Dark Matter Halo. 3 2024.
- [118] Lucas G. Collodel, Daniela D. Doneva, and Stoytcho S. Yazadjiev. Circular Orbit Structure and Thin Accretion Disks around Kerr Black Holes with Scalar Hair. *Astrophys. J.*, 910(1):52, 2021.
- [119] Haiyuan Feng, Miao Li, Gui-Rong Liang, and Rong-Jia Yang. Adiabatic accretion onto black holes in Einstein-Maxwell-scalar theory. *JCAP*, 04(04):027, 2022.
- [120] Yingdong Wu, Haiyuan Feng, and Wei-Qiang Chen. Thin accretion disk around black hole in Einstein–Maxwell-scalar theory. *Eur. Phys. J. C*, 84(10):1075, 2024.
- [121] Yu-Xiang Huang, Sen Guo, Yu-Hao Cui, Qing-Quan Jiang, and Kai Lin. Influence of accretion disk on the optical appearance of the Kazakov-Solodukhin black hole. *Phys. Rev. D*, 107(12):123009, 2023.